minerals

MDPI

Article

Petrogenesis of the Helong Granites in Southern Jiangxi Province, China: Constraints from Geochemistry and In Situ Analyses of Zircon U–Pb–Hf Isotopes

Xinxing Liu [1], Weixin Shi [2,*], Juan Zhang [1,*], Xiaoyan Zhang [1], Junfeng Yang [1] and Wei Li [3]

[1] Hebei Key Laboratory of Strategic Critical Mineral Resources, Hebei GEO University, Shijiazhuang 050031, China
[2] Cores and Samples Center of Natural Resources, China Geological Survey, Beijing 100192, China
[3] The Seventh Geological Brigade of Jiangxi Bureau of Geology, Key Laboratory of Ionic Rare Earth Resources and Environment, Ganzhou 341000, China
* Correspondence: shiweixincugb@163.com (W.S.); zhangjqtds@126.com (J.Z.)

Abstract: The Jinzhuping and Changkeng granites are related to the Helong W–Sn ore field in southern Jiangxi Province, China. Three different phases can be found in the Jinzhuping pluton, and their LA-ICP-MS zircon U–Pb ages are 155.2 ± 0.68 Ma, 154.0 ± 0.56 Ma, and 153.4 ± 0.99 Ma, respectively, indicating two types of granitic rocks. All granites in the Helong ore field have similar geochemical characteristics, they have high contents of SiO_2 (73.99 wt.%–77.68 wt.%), and total alkali (7.56 wt.%–8.76 wt.%) and are weakly to strongly peraluminous. They are slightly enriched in HREE and depleted in Eu, Ba, Sr, P, and Ti. Zircon εHf(t) values of the Jinzhuping three granites are from −14.4 to −10.4, from −15.3 to −11.4, and from −18.1 to −10.5, and the Hf TDM model ages range from 1.83 to 2.06 Ga, from 1.89 to 2.14 Ga, and from 1.83 to 2.31 Ga, respectively. Whole-rock geochemistry and Hf isotope analysis indicate that the Helong granites experienced a high degree of differentiation and evolution derived by partial melting of the Late Paleoproterozoic crustal materials, and they formed in a backarc caused by low-angle subduction of the Paleopacific plate.

Keywords: LA-ICP-MS zircon U–Pb dating; geochemistry; in situ zircon Hf isotopes; Helong granites; Southeastern China

check for updates

Citation: Liu, X.; Shi, W.; Zhang, J.; Zhang, X.; Yang, J.; Li, W. Petrogenesis of the Helong Granites in Southern Jiangxi Province, China: Constraints from Geochemistry and In Situ Analyses of Zircon U–Pb–Hf Isotopes. *Minerals* **2023**, *13*, 101. https://doi.org/10.3390/min13010101

Academic Editor: Rubén Díez-Fernández

Received: 24 November 2022
Revised: 24 December 2022
Accepted: 5 January 2023
Published: 9 January 2023

Copyright: © 2023 by the authors. Licensee MDPI, Basel, Switzerland. This article is an open access article distributed under the terms and conditions of the Creative Commons Attribution (CC BY) license (https://creativecommons.org/licenses/by/4.0/).

1. Introduction

The Nanling Range is one of the world's largest W–Sn metallogenic provinces in the South China Block [1], which hosts the majority of the mineralization with about 9.943 million tons of WO_3 and 6.561 million tons of Sn [2]. The eastern Nanling Range, (southern Jiangxi Province) presents a high density of W-dominant deposits with diverse metal associations (Sn, Mo, Bi, Cu, Ag, Sb, Hg, and rare earth elements), which are thought to be closely related to Mid-Late Mesozoic composite plutons (Figure 1) [2–6]. High-silica granites, associated with W-dominant and rare-metal deposits in southern Jiangxi, belong to high-K calc-alkaline and weakly peraluminous series, with pronounced negative Eu anomalies and are highly fractionated [7–16]. Previous studies have shown that the W–Sn-related granites in southern Jiangxi Province mostly resulted from partial melting of Mesoproterozoic to Paleoproterozoic crustal materials [1,17–20]. However, the dynamic background of the granitic plutons remains controversial, including two perspectives: (1) related to the syn-collision to post-collision stages after the closure of Paleotethys in the Early Yanshanian [21–24], (2) related to the back-arc extension associated with Paleopacific subduction in the Middle-Late Jurassic [25–29].

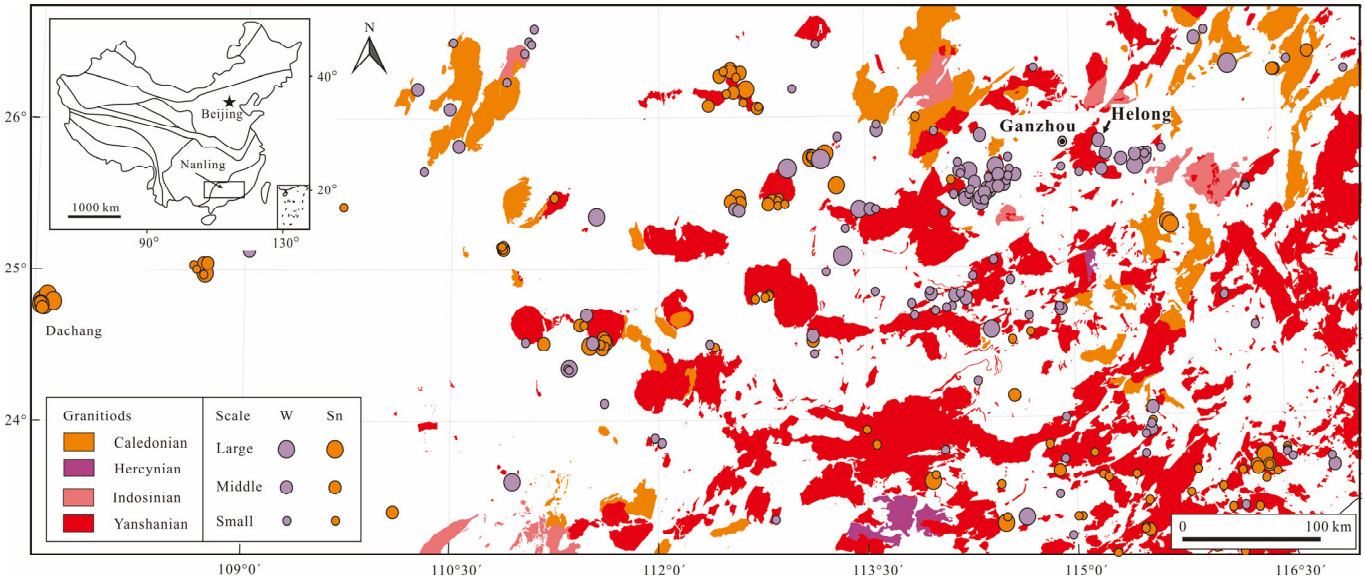


Figure 1. Distribution map of granitoids and major Mesozoic W–Sn deposits in Nanling region (modified from [4]).

The Helong ore field, with W–Sn reserves of 15,000 tons and 9500 tons, respectively, is one of the W–Sn metallogenic prospects in southern Jiangxi Province (Figure 1) [29,30]. Many deposits in the Helong ore field formed during the Late Jurassic, as shown by recent wolframite and cassiterite U–Pb, molybdenite Re–Os, and mica Ar–Ar dating (ca. 160–150 Ma) [5,6,29,31]. The consistent isotope ages between the W–Sn deposits and the adjacent granites indicate a genetic link between them. However, the petrogenesis, chemical composition, and dynamic background of these Late Jurassic granites remain to be unclear.

In this paper, we present a detailed study on the petrology, mineralogy, whole-rock major and trace elements, and zircon U–Pb–Hf characteristics of the Jinzhuping and Changkeng granites in the Helong ore field. Combined with the corresponding published data, we constrain the petrogenesis of the Jinzhuping and Changkeng granites, and furthermore discuss the dynamic background of the plutonism in the southern Jiangxi Province.

2. Geological Setting of the Helong Ore Field and Petrology of the Granites

2.1. Geological Setting

The Helong orefield is located in Jiangxi Province, South China (Figure 1); geologically, the orefield is located in the Nanling tungsten belt [2,29]. The Nanling tungsten belt overlaps the EW-trending Nanling Range, which is composed of the Yuecheng, Doupang, Mengzhu, Qitian, and Dayu mountain belts that separate the Yangtze River and Zhujiang River systems [2]. Except for some scattered Late Triassic deposits, Late Jurassic deposits are the main W and Sn deposits in the Nanling tungsten belt [2,6,18,32–36]. Most granites in the region were formed coevally with the Late Jurassic W–Sn deposits, which occurred at a peak of ca. 160 to 150 Ma [5,6,28,33–35].

The Helong orefield is hosted in the junction of the E-W-trending complex structure belt of the middle and eastern Nanling region and the NNE-SSW-trending Wuyi uplifted zone [29]. Stratigraphic sequences exposed in the orefield include Chinese stage for the Sinian to Cambrian marine clastic rocks that are low-grade metamorphosed and extremely thick, Devonian to Permian marine to continental clastic and carbonate rocks, and Jurassic to Tertiary continental clastic rocks [29]. Mesozoic granites are dominant in the orefield, including the Dabu composite pluton, and many minor intrusions such as the Tieshanlong, Anqiantan, Jinzhuping, and Changkeng granites (Figure 2) [29,30]. These igneous rocks were mainly intruded during two periods, i.e., the Caledonian (ca. 423–430 Ma) and the Late Mesozoic (ca. 161–153 Ma) [29,37–39]. The W-polymetallic ore deposits associated with the Late Jurassic granites, which take the form of quartz vein, porphyry, skarn, and greisen type,

are the Laikeng, Tongziping, Niushikeng, Changkeng, and Jinzhuping deposits, as shown in Figure 2. Importantly, the Jinzhuping and Changkeng granites have been associated with the W-dominant deposits in time, space, and genesis in the Helong orefield [5,6,29].

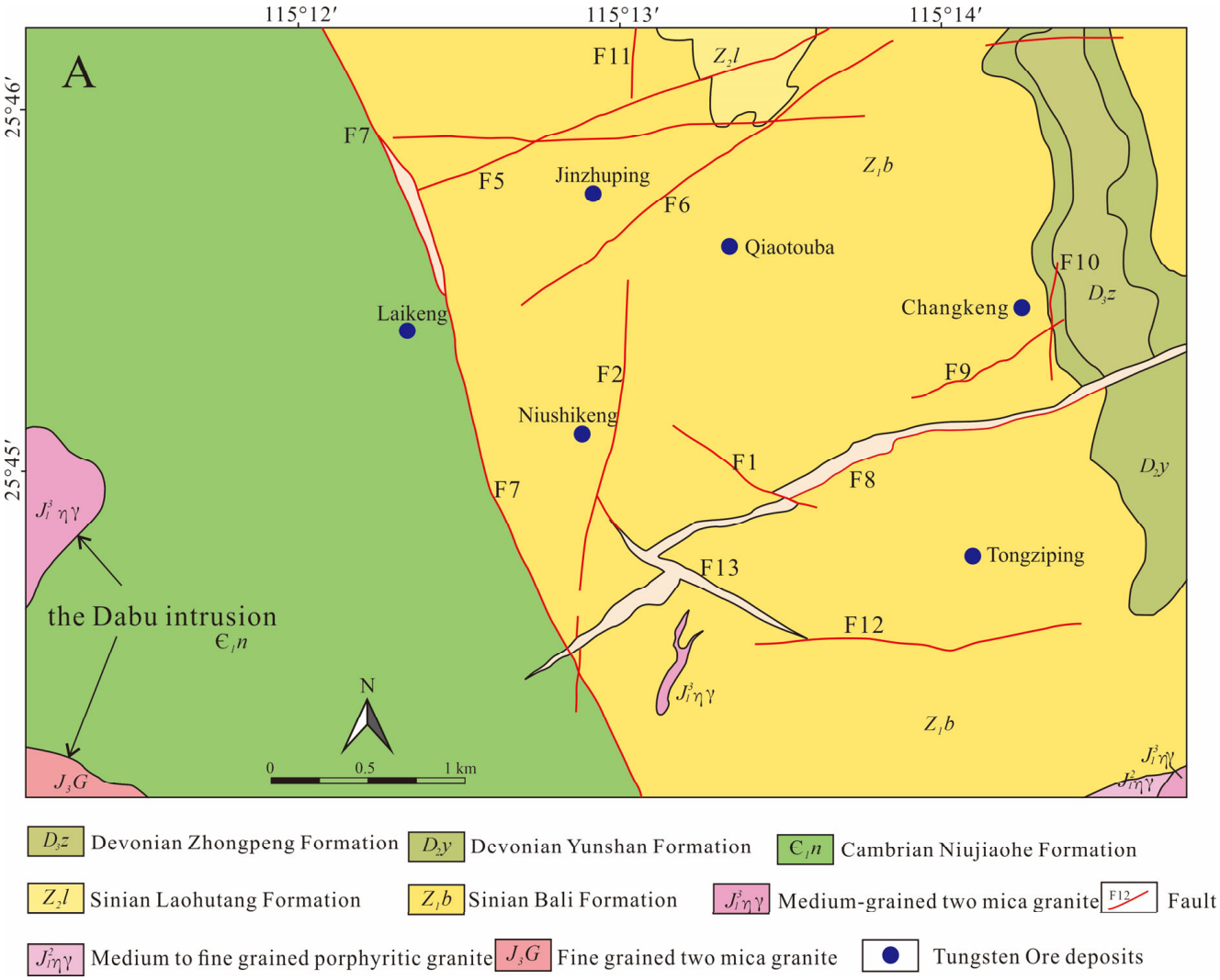


Figure 2. Geological map of the Helong ore field (modified from [5]).

Drill cores show that the main phase of Jinzhuping granites is medium- to coarse-grained biotite granite, which intrudes into the Cambrian metamorphic clastic rocks and hosts most of the ore bodies of the Jinzhuping deposit [5]. The main-phase granite (Figure 3A–E) is replaced by porphyritic biotite granite in the top (Figure 3F–H) and cut through by aplite (Figure 3I–K). The Changkeng granite consists predominantly of the main-phase biotite granite (Figure 3L–N), and in this ore deposit, the quartz-wolframite veins occur directly within the Sinian metasandstone and slate [29]. Detailed petrological descriptions of the four granites are presented in the next section.

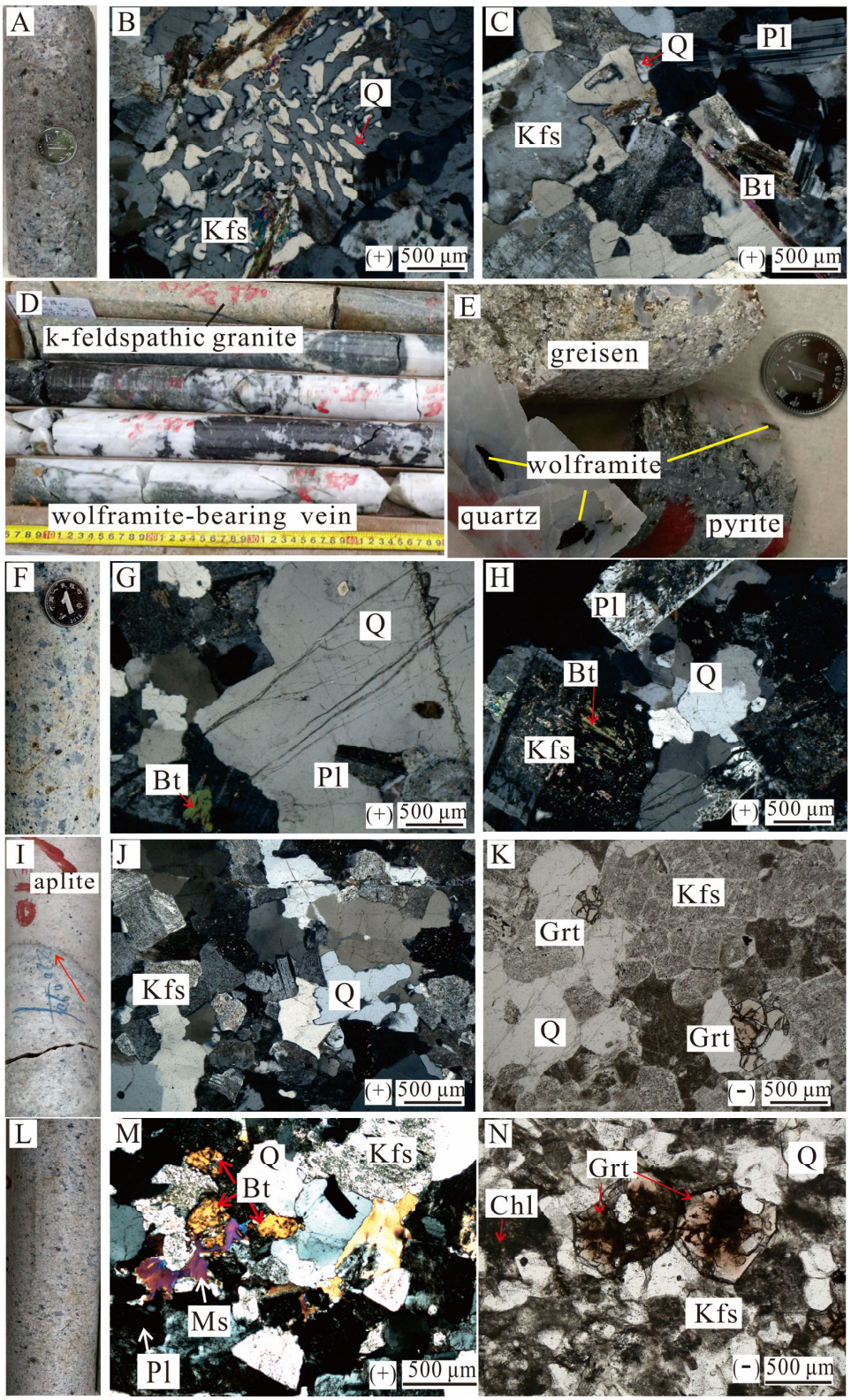


Figure 3. Photographs showing mineral composition of granites associated with the Jinzhuping (**A**–**K**) and Changkeng (**L**–**N**) ore deposits. (**A**–**C**) Medium- to coarse-grained biotite granite; (**D**–**E**) potash feldspathization, greisenization, and wolframite-quartz vein in the main-phase granite; (**F**–**H**) porphyritic biotite granite; (**I**–**K**) aplite; (**L**–**N**) mineral composition of biotite granite, and the K-feldspar replaced by chlorite. Q—quartz; Pl—plagioclase; Kfs—potassium feldspar; Bt—biotite; Ms—muscovite; Grt—garmet; Chl—chlorite.

2.2. Petrology of the Ore-Hosting Granites

2.2.1. The Jinzhuping Granites

The main-phase granite occupies about 90% of the total pluton, while the porphyritic granite is mostly distributed in the top zone of the pluton, occupying about 6% of the total pluton (Figure 3A–F). The aplite that cuts through the main-phase granite (Figure 3I) is only visible in part of the drill cores, with a very small percentage. W–Sn mineralization occurs mainly in the main-phase granite (Figure 3D–E), followed by porphyritic granite, but no mineralization is found in aplite.

The main-phase granites are dominated by medium- to coarse-grained biotite granite (Figure 3A–C), and consist mainly of alkali feldspar (25–30 vol%), plagioclase (25–30 vol%), quartz (25–38 vol%), biotite (5–8 vol%), and muscovite (0–4 vol%) with accessory magnetite, zircon, apatite, ilmenite, titanite, hematite, and fergusonite. Hydrothermal minerals (mainly wolframite, cassiterite, chalcopyrite, pyrite, and scheelite) are widespread. Quartz is mainly present as anhedral grains (Figure 3B–C). K-feldspars are mainly subhedral granular perthite potassium feldspar, and they generally include fine-grained anhedral quartz (Figure 3B). Plagioclase is euhedral to subhedral (Figure 3C), and enclosed abundant tiny sericite. The biotite is euhedral to subhedral and coexists with K-feldspar and quartz (Figure 3C).

The texture varies into porphyritic in the top of the main-phase granite and the porphyritic granite is grayish white (Figure 3F). Abundant potassium feldspar megacrysts, usually euhedral to subhedral, are embedded in a moderately coarse groundmass of feldspars and quartz, and enclose abundant biotite and quartz (Figure 3G). The irregular or rounded quartz grains may reach 6 mm in diameter (Figure 3G). The flakes of muscovite, frequently clustered together, and enclose euhedral to subhedral garnet. The porphyritic biotite granite consists mainly of alkali feldspar (27–32 vol%), plagioclase (22–30 vol%), quartz (23–36 vol%), biotite (4–6 vol%), and varying muscovite (0–2 vol%) with accessory zircon, apatite, hematite, and fergusonite.

The aplite is mainly fine grained, light grey to light red (Figure 3I), and mainly comprises quartz (35–38 vol%), K-feldspar (40–45 vol%), plagioclase (15–18 vol%), biotite (3–5 vol%), and garnet (1–4 vol%), with accessory zircon, limonite, ilmenite, and cassiterite. Quartz is mainly present as subhedral to anhedral grains (Figure 3J–K). K-feldspar is mainly subhedral granular perthite, and it generally includes fine-grained euhedral plagioclase and tiny muscovite and is altered by clay minerals (Figure 3K). Plagioclase is euhedral to subhedral. The euhedral to subhedral garnets mostly occur interstitially between K-feldspar and quartz (Figure 3K). Muscovite is mostly present as subhedral fine- to medium-grained flakes.

2.2.2. The Changkeng Granite

The main-phase granite is dominated by medium- to coarse-grained biotite granite (Figure 3L) and consist mainly of K-feldspar (20–25 vol%), plagioclase (20–25 vol%), quartz (30–35 vol%), biotite (5–9 vol%), and muscovite (0–2 vol%) (Figure 3M–N) with accessory zircon, garnet (Figure 3N), titanite, and fluorite. Quartz is mainly present as anhedral grains (Figure 3M–N). K-feldspars are subhedral to anhedral, and generally, altered by chlorite and clay minerals (Figure 3M–N). Plagioclase is euhedral to subhedral (Figure 3M), and encloses abundant tiny sericite. The mainly subhedral biotite mostly occurs interstitially between K-feldspar and quartz (Figure 3M). Muscovite is mostly present, enclosed in K-feldspar as fine-grained flakes or occurs interstitially between biotite and quartz (Figure 3M). The subhedral to anhedral garnet mostly occurs interstitially between K-feldspar and quartz (Figure 3N).

3. Samples and Analytical Methods

3.1. Sampling

Samples of main-phase granite, porphyritic granite, and aplite in the Jinzhuping deposit, i.e., JZP-6, JZP-12, and JZP-33, for zircon U–Pb dating and Hf isotopes analyses were collected from drill core Zk4105 at depths of 525 m, 430 m, and Zk3305 at 610 m, respectively. Samples of the four granites, i.e., from JZP60-1 to JZP60-8, from JZP61-1 to JZP61-6, from JZP62-1 to JZP62-7, and from CK60-1 to CK60-7 for whole rock major and trace element analyses were collected from different depths of drill core Zk4105, Zk3305, Zk3301 in Jinzhuping, and Zk311 in Changkeng, respectively.

3.2. Whole Rock Major and Trace Element Analyses

The major and trace element analysis for the bulk rock samples was mainly carried out in the Yanduzhongshi Geological Analysis Laboratories Ltd. (103 Beiqing Road, Haidian District, Beijing). First, fresh samples were broken to centimeter sizes; only the fresh pieces were selected, washed with deionized water, dried, and then ground to less than 200 mesh (0.5200 ± 0.0001 g) for geochemical analyses. Sample powders were fluxed with $Li_2B_4O_7$ (1:8) to make homogeneous glass disks at 1250 °C using a V8C automatic fusion machine produced by the Analymate Company in China. The bulk rock's major elements were analyzed using X-ray fluorescence spectrometry techniques (Zetium, PANalytical, or XRF-1800, Shimadzu). The analytical errors for major elements were better than 1%. For trace element analysis, first, sample powders were dissolved using distilled HF + HNO_3 in a screw-top Teflon beaker for 4 days at 100 °C. The trace elements of those samples were analyzed by inductively coupled mass spectrometry (ICP-MS) at the Yanduzhongshi Geological Analysis Laboratories Ltd. The analytical uncertainty of the elements examined here was better than 5% for ICP-MS analysis, except for a few samples with low contents of trace elements, for which the uncertainty was about 10%. The obtained values of trace elements in the GSR-2 standard are all consistent with their recommended values.

3.3. Zircon LA-ICP-MS In Situ U–Pb Dating Method

The zircon U–Pb isotope analysis was carried out in situ by using a NWR193 laser-ablation microprobe (Elemental Scientific Lasers LLC), attached to a Analytikjena M90 at the Yanduzhongshi Geological Analysis Laboratories Ltd. In order to adjust sensitivity, helium was used as a carrier gas and argon gas was used as a compensation gas during the laser ablation process, and both were mixed by a Y-shaped junction before entering ICP. Every time-resolved analysis includes an approximately 20–30 s blank signal and a 40 s sample signal. Off-line processing of data was completed using the software ZSkits, including selection of samples and blank signals, drift correction of instrument sensitivity, calculations for elemental contents, and U–Th–Pb isotope ratios and ages.

Isotopic fractionation correction for U–Pb dating was carried out using zircon standard 91500 as an external standard. When 5–10 sample points were completed, 91500 was analyzed twice using one Plesovice analytical point as a monitor. The calculation of weighted average ages and plotting of the concordia diagram were completed with Isoplot/Ex_ver3 [40], and the common lead adjustment was conducted using the Andersen software [41]. According to the actual situation, the tested denuded diameter was selected as 30 μm. The standard sample 91500 and Plesovice both coincided with values recommended [42,43].

3.4. In Situ Zircon Hf Isotopic Analyses

Zircon Lu–Hf isotope analysis was carried out in situ by using a NWR193 laser-ablation microprobe (Elemental Scientific Lasers LLC), attached to a Neptune multicollector ICP-MS at the Yanduzhongshi Geological Analysis Laboratories Ltd. Instrumental conditions and data acquisition were comprehensively described by Wu et al. [44]. For the current analyses, a stationary spot with a beam diameter of 40 μm was used. Helium was used as carrier gas to transport the ablated sample from the laser-ablation cell to the ICP-MS torch via a mixing

chamber mixed with argon. In order to correct the isobaric interferences of ^{176}Lu and ^{176}Yb on ^{176}Hf, ^{176}Lu/^{175}Lu = 0.02658 and ^{176}Yb/^{173}Yb = 0.796218 ratios were determined (e.g., Chu et al. [45]). For instrumental mass bias correction, Yb isotope ratios were normalized to ^{172}Yb/^{173}Yb of 1.35274 (e.g., Chu et al. [45]) and Hf isotope ratios to ^{179}Hf/^{177}Hf of 0.7325 using an exponential law. The mass bias behavior of Lu was assumed to follow that of Yb, and mass bias correction protocol details were described by Wu et al. [44]. Zircon 91500 and Plesovice were used as the reference standards during our routine analyses. Initial ^{176}Hf/^{177}Hf ratios εHf (t) were calculated with reference to the chondritic reservoir (CHUR) of Blichert-Toft and Albarede [46] at the time of zircon growth from the magma. The single-stage Hf model age (TDM1) was calculated relative to the depleted mantle with present-day ^{176}Hf/^{177}Hf = 0.28325 and ^{176}Lu/^{177}Hf = 0.0384 (e.g., Griffin et al. [47]).

4. Results

4.1. Whole-Rock Major and Trace Element Compositions

The whole-rock major and trace elements were measured in 28 samples from Helong granites and the results are given in Table 1. All granites have very high SiO_2 contents in the range 73.99%–77.68% (Figure 4A) and very similar geochemical characteristics. The Helong granite plots in the high-K field in terms of K_2O vs. SiO_2 (Figure 4B), and the granites are weakly to strongly peraluminous, with A/CNK values from 0.92 to 1.13 (Figure 4). In the Harker diagrams (Figure 5), they show similar geochemical trends. In the REE and trace element distribution patterns (Figure 6), they are most depleted in LREEs and Eu, but are enriched in HREEs, while the chondrite-normalized REE patterns of most porphyritic granite samples are nearly flat. Specifically, the Changkeng granite has lower Eu/Eu* ratios (0.03–0.05) relative to the Jinzhuping granites (the main-phase granite 0.01–0.09, the porphyritic granite 0.01–0.13, and the late-stage aplite 0.03–0.16), while the Jinzhuping porphyritic granite has higher $(La/Yb)_N$ values (from 0.14 to 1.04) relative to the Jinzhuping main-phase granite (from 0.08 to 0.48), the Jinzhuping late-stage aplite (from 0.13 to 0.21), and the Changkeng granite (from 0.16 to 0.47). In addition, the depletion in Eu in the Jinzhuping main-phase granite is stronger than that in the other granites, while the intensities of the depletions in Ba, Sr, P, and Ti were almost uniform in all granites.

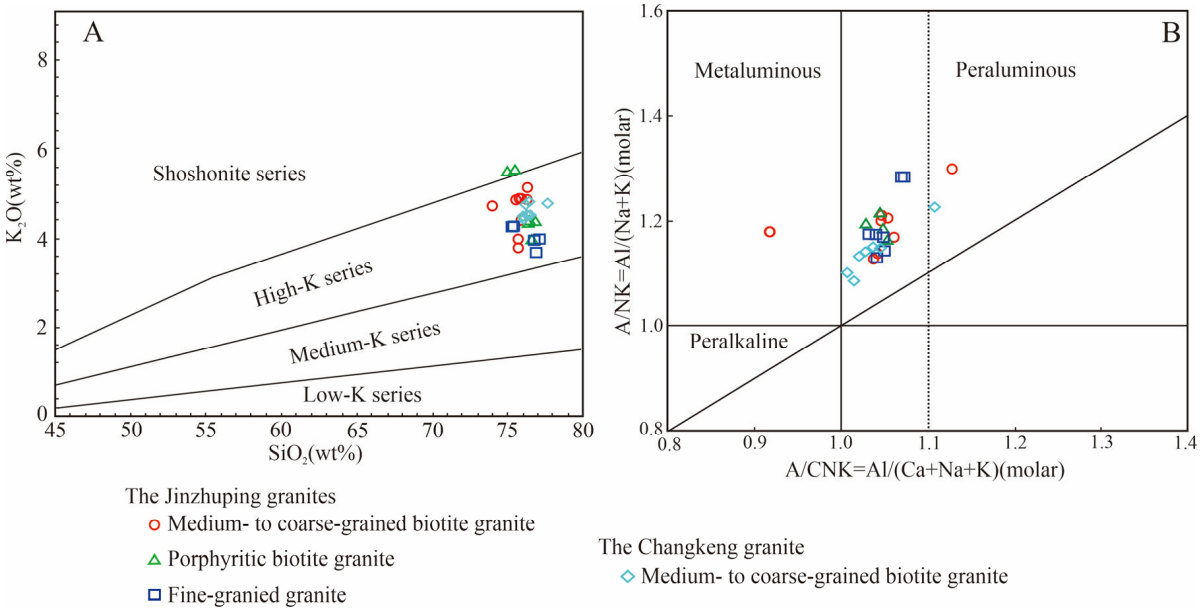


Figure 4. Pl SiO_2 vs. K_2O diagram (**A**) and A/NK vs. A/CNK diagrams (**B**) of the Helong granities (the compositional fields are from Rollinson [48] and Streckeisen and Le Maitre [49], respectively).

Table 1. Major and trace element compositions of the Helong granites.

Sample Numbers	JZP-60-1	JZP-60-2	JZP-60-3	JZP-60-5	JZP-60-6	JZP-60-7	JZP-60-8	JZP-60-9	JZP-61-1	JZP-61-2	JZP-61-3	JZP-61-5	JZP-61-6	JZP-61-8	JZP-62-1	JZP-62-2	JZP-62-3	JZP-62-5	JZP-62-6	JZP-62-7	JZP-62-8	CK-60-1	CK-60-3	CK-60-4	CK-60-5	CK-60-6	CK-60-7	CK-60-8
SiO_2	76.33	75.96	73.99	75.68	75.92	75.72	76.33	75.57	76.8	76.45	75.02	76.58	76.56	75.51	77.01	76.92	77.15	75.3	75.33	76.47	76.36	77.68	76.37	76.07	76.19	76.46	76.4	76.07
TiO_2	0.01	0.02	0.02	0.01	0.02	0.02	0.02	0.01	0.02	0.03	0.01	0.01	0.02	0.01	0.02	0.02	0.01	0.01	0.01	0.01	0.01	0.02	0.01	0	0.01	0	0	0
Al_2O_3	13.03	13.07	12.26	12.73	12.91	13.16	12.77	13.1	12.87	12.64	12.82	13.26	13.28	13.03	12.6	12.5	12.86	12.9	12.86	13.02	12.93	12.08	12.59	12.76	12.69	12.47	12.19	12.64
TFe_2O_3	0.99	0.84	1.07	0.75	1.29	0.82	0.66	0.63	0.98	0.96	0.87	0.75	0.74	0.86	0.82	0.8	0.67	0.62	0.63	0.69	0.69	0.37	0.92	0.83	0.46	0.77	1.14	0.87
MnO	0.06	0.16	0.27	0.14	0.1	0.36	0.22	0.09	0.08	0.08	0.1	0.19	0.19	0.1	0.62	0.62	0.24	0.1	0.1	0.22	0.22	0.15	0.28	0.1	0.16	0.09	0.18	0.13
MgO	0.07	0.14	0.08	0.14	0.14	0.08	0.08	0.14	0.14	0.13	0.12	0.06	0.07	0.11	0.11	0.1	0.07	0.15	0.13	0.07	0.07	0.08	0.09	0.1	0.08	0.08	0.08	0.09
CaO	0.58	0.85	1.64	0.85	0.62	0.55	0.58	0.83	0.79	0.77	0.85	0.63	0.62	0.85	0.75	0.76	0.61	1.09	1.1	0.56	0.56	0.42	0.59	0.7	0.57	0.66	0.58	0.67
Na_2O	3.58	3.69	3.19	3.84	3.47	4.5	3.6	2.92	3.71	3.7	2.99	4.38	4.37	3	4.09	4.1	4.14	3.3	3.28	3.95	3.9	3.61	3.67	3.79	3.88	3.71	2.86	3.77
K_2O	5.18	4.43	4.76	3.99	4.92	3.82	4.88	4.9	4.4	4.39	5.52	3.99	3.99	5.54	3.71	3.7	4.01	4.26	4.29	4.54	4.52	4.82	4.55	4.46	4.79	4.55	4.85	4.53
P_2O_5	0.03	0.03	0.03	0.03	0.03	0.03	0.03	0.03	0.04	0.03	0.03	0.03	0.03	0.03	0.03	0.03	0.03	0.03	0.03	0.03	0.03	0.03	0.03	0.03	0.03	0.03	0.03	0.03
LOI	0.65	1.09	2.01	1.58	0.71	0.69	1.02	1.54	0.63	0.67	1.22	0.59	0.63	1.27	0.66	0.68	0.63	1.89	1.97	0.69	0.72	0.73	0.82	1.03	1	1.11	1.3	0.9
TOTAL	100.5	100.28	99.31	99.73	100.14	99.74	100.19	99.76	100.45	99.84	99.55	100.47	100.5	100.31	100.42	100.22	100.43	99.66	99.73	100.25	99.99	99.98	99.94	99.88	99.86	99.94	99.61	99.68
A/CNK	1.04	1.05	0.92	1.05	1.06	1.05	1.04	1.13	1.05	1.03	1.03	1.05	1.05	1.04	1.04	1.03	1.05	1.07	1.07	1.05	1.05	1.01	1.05	1.04	1.01	1.02	1.11	1.03
Rb	525	500	699	523	530	604	608	656	503	499	675	619	615	670	461	468	521	552	559	577	583	440	428	488	447	486	479	434
Ba	16.64	18.34	8.89	12.22	4.91	2.13	5.45	11.84	47.56	45.66	36.33	4.96	4.8	37.71	41.88	49.77	8.13	11.52	12.2	6.46	6.31	28.36	12.89	19.9	28.17	18.37	15.79	13.52
Th	17.18	26.46	13.89	15.34	20.23	12.02	10.95	13.5	22.38	24.2	19.28	14.49	19.93	18.17	12.46	12.79	25.64	14.78	12.33	21.56	18.95	14.18	17.96	19.83	20.39	23.87	13.26	20.27
U	24.83	30	28.26	32.8	28.28	34.42	30.32	27.68	15.52	19.5	14.87	30.65	34.68	14.71	31.38	30.42	37.63	25.3	24.09	32.96	29.79	27.6	28.95	23.2	28.01	26.71	20.36	28.74
Nb	13.35	12.67	20.18	10.91	12.21	6.34	16.44	9.94	15.95	15.76	11.65	11.73	12.81	11.43	8.68	9.12	20.82	14.99	12.52	16.17	14.01	6.89	11.74	14.16	9.63	11.65	11.04	12.65
Ta	7.11	9.34	1.5	10.3	16.23	12.21	11.98	10.03	8.35	6.86	6.64	14.06	17.44	6.63	5.3	5.11	19.41	8.77	9.02	10.85	10.22	9.93	11.15	9.1	9.86	7.87	10.25	10.56
K	171.93	147.01	158.04	132.54	163.5	126.69	162.06	162.55	146.07	145.65	183.31	132.39	132.5	183.83	123.28	122.99	133.05	141.55	142.39	150.67	150.11	159.95	151.24	148.2	159.09	151.11	161.11	150.43
La	6.24	6.48	5.11	4.49	3.32	4.2	6.54	4.96	10	10.17	6.49	4.45	4.9	6.31	6.35	6.69	6.47	3.95	3.5	5.62	6.14	3.2	5.27	7.39	4.4	5.78	5.12	5.14
Ce	17.08	17.23	18.17	12.02	10.05	10	19.39	12.07	24.23	24.34	16.65	12.02	13.06	16.19	14.49	15.78	20.66	11.46	10.24	16.45	17.23	7.79	14.46	19.1	10.76	15.3	13.26	13.24
Sr	9.16	23.2	16.41	16.71	7.04	4.02	5.42	11.41	28.24	27.37	16.03	3.98	4.16	15.69	27.81	28.1	8.39	21.75	22.3	7.19	7.01	10.98	10.95	13.29	10.1	13.45	8.95	10.02
P	117	130	142	126	122	129	120	143	156	147	137	131	136	133	116	126	138	121	122	131	121							
Nd	13.35	12.67	20.18	10.91	12.21	6.34	16.44	9.94	15.95	15.76	11.65	11.73	12.81	11.43	8.68	9.12	20.82	14.99	12.52	16.17	14.01	6.89	11.74	14.16	9.63	11.65	11.04	12.65
Zr	81.48	114.11	53.44	82.4	78.07	86.28	67.73	74.73	64.68	80.37	74.21	132.67	142.31	70.37	74.01	75.84	112.42	79.4	45.17	113.88	90.65	75.29	85.26	76.61	86.58	72.27	75.92	70.6
Hf	5.6	8.2	4.63	7.16	7.46	7.54	6.11	5.89	4.65	5.25	4.54	10.73	11.78	4.54	9.09	9.44	9.11	6.25	3.76	9.07	6.89	6.14	6.57	5.4	6.21	5.64	5.81	5.54
Sm	5.59	4.67	12.2	5.41	7.21	2.93	8.31	5.22	4.89	4.72	4.11	6.74	7.36	4.16	3.12	3.35	14.61	11.05	8.03	9.5	7.63	4.03	5.32	6.28	4.62	5.07	4.63	6.8
Eu	0.07	0.15	0.04	0.04	0.05	0.02	0.02	0.05	0.23	0.2	0.16	0.03	0.03	0.17	0.21	0.19	0.03	0.05	0.05	0.03	0.02	0.06	0.06	0.1	0.06	0.08	0.06	0.08
Ti	65.33	97.09	98.89	85.71	113.28	104.29	98.89	82.11	122.27	150.44	77.32	88.7	89.9	72.52	148.04	116.27	55.14	64.73	91.7	67.13	84.51	98.29	41.36	9.59	67.73	10.19	17.98	15.58
Gd	6.28	5.9	13.94	7.1	8.89	5.97	10.38	7.23	5.54	5.21	5.23	9.17	9.64	5.07	5.33	5.34	16.83	13.71	9.98	12.24	9.56	6.1	7.02	7.32	6.38	6.7	5.83	8.48
Dy	13.54	14.03	27.53	17.87	19.3	26.29	25.2	15.12	10.35	9.41	10.55	22.91	25.76	10.45	23.43	23.53	34.38	24.32	19	26.71	21.79	13.84	19.47	14.57	15.3	13.58	12.93	17.82
Er	8.48	12.63	17.59	12.36	12.27	24.47	17.54	9.34	6.34	5.87	6.34	16.89	18.87	6.42	21.43	21.78	19.67	12.27	10.62	17.81	15.83	8.99	16.3	8.97	10.73	8.84	9.14	11.13
Yb	9.34	21.48	23.08	15.04	15.31	37	23.15	9.43	7.27	7.02	7.41	21.83	24.57	7.4	36.03	36.36	26.37	13.81	12.9	23.26	21.9	11.89	23.2	11.32	13.21	10.08	12.61	13.73
Lu	1.58	4.08	3.98	2.79	2.96	6.96	4.02	1.57	1.28	1.24	1.27	3.92	4.31	1.31	6.67	6.82	4.7	2.4	2.22	4.13	3.88	2.09	4.13	1.92	2.43	1.68	2.24	2.39
Y	92.42	130.56	216.72	142.01	156.3	262.24	200.71	116.57	74.35	72.16	74.21	179.87	197.37	71.09	247.88	254.37	260.87	135.6	121.28	207.22	181.32	110.51	176.19	109.58	120.05	107.27	108.64	131.81
Pr	2.67	2.56	3.15	2.06	2	1.39	3.04	1.96	3.19	3.18	2.37	2.12	2.31	2.31	1.98	2.12	3.46	2.36	2.03	2.83	2.67	1.25	2.23	2.86	1.86	2.26	2.14	2.3
Tb	1.8	1.79	3.69	2.29	2.65	2.62	3.15	2.21	1.42	1.29	1.36	2.88	3.21	1.37	2.3	2.28	4.88	3.43	2.81	3.4	2.87	1.91	2.3	2.09	1.98	1.93	1.7	2.48
Ho	2.89	3.54	6.01	4.01	4.07	6.82	5.63	3.38	2.18	2	2.18	5.32	5.95	2.2	6.25	6.31	6.75	4.54	3.71	5.79	4.91	3.3	4.89	3.28	3.51	3.18	3.1	3.76
Tm	1.44	2.91	3.2	2.38	2.43	5.12	3.31	1.5	1.11	1.05	1.11	3.16	3.5	1.13	4.71	4.74	3.62	2.19	1.98	3.29	3.17	1.79	3.17	1.71	2.09	1.56	1.83	2.1
∑REE	183	241	375	241	259	402	347	201	168	164	151	303	334	147	389	399	444	256	221	354	313	184	296	211	207	195	194	234
Eu/Eu*	0.04	0.09	0.01	0.02	0.02	0.01	0.01	0.02	0.13	0.12	0.11	0.01	0.01	0.11	0.16	0.14	0.01	0.01	0.02	0.01	0.01	0.04	0.03	0.05	0.03	0.04	0.04	0.03
$(La/Yb)_N$	0.48	0.22	0.16	0.21	0.16	0.08	0.2	0.38	0.99	1.04	0.63	0.15	0.14	0.61	0.13	0.13	0.18	0.21	0.19	0.17	0.2	0.19	0.16	0.47	0.24	0.41	0.29	0.27
Th/U	0.69	0.88	0.49	0.47	0.72	0.35	0.36	0.49	1.44	1.24	1.3	0.47	0.57	1.24	0.4	0.42	0.68	0.58	0.51	0.65	0.64	0.51	0.62	0.85	0.73	0.89	0.65	0.71
Ba/Rb	0.03	0.04	0.01	0.02	0.01	0	0.01	0.02	0.09	0.09	0.05	0.01	0.01	0.06	0.09	0.11	0.02	0.02	0.02	0.01	0.01	0.06	0.03	0.04	0.06	0.04	0.03	0.03
Rb/Sr	57.31	21.57	42.62	31.29	75.27	150.29	112.05	57.49	17.82	18.22	42.1	155.72	147.95	42.69	16.58	16.64	62.05	25.38	25.08	80.21	83.13	40.06	39.06	36.69	44.27	36.16	53.51	43.29
Sm/Nd	0.42	0.37	0.6	0.5	0.59	0.46	0.51	0.53	0.31	0.3	0.35	0.57	0.57	0.36	0.36	0.37	0.7	0.74	0.64	0.59	0.54	0.58	0.45	0.44	0.48	0.44	0.42	0.54
Nd/Ta	1.88	1.36	13.48	1.06	0.75	0.52	1.37	0.99	1.91	2.3	1.76	0.83	0.73	1.72	1.64	1.79	1.07	1.71	1.39	1.49	1.37	0.69	1.05	1.56	0.98	1.48	1.08	1.2
Zr/Hf	14.56	13.91	11.53	11.5	10.47	11.44	11.09	12.69	13.9	15.3	16.35	12.37	12.08	15.5	8.14	8.04	12.34	12.7	12.02	12.55	13.15	12.26	12.97	14.17	13.93	12.82	13.06	12.75
K/Rb	81.85	73.44	56.49	63.37	77.15	52.41	66.69	61.96	72.58	72.99	67.91	53.43	53.85	68.63	66.84	65.73	63.86	64.1	63.64	65.29	64.39	90.93	86.65	81.56	84.46	82.8	78.55	
K/Ba	2584	2003	4447	2712	8327	14867	7433	3431	768	797	1261	6677	6899	1219	736	618	4094	3072	2917	5831	5946	1410	2874	1998	1341	2192	2382	

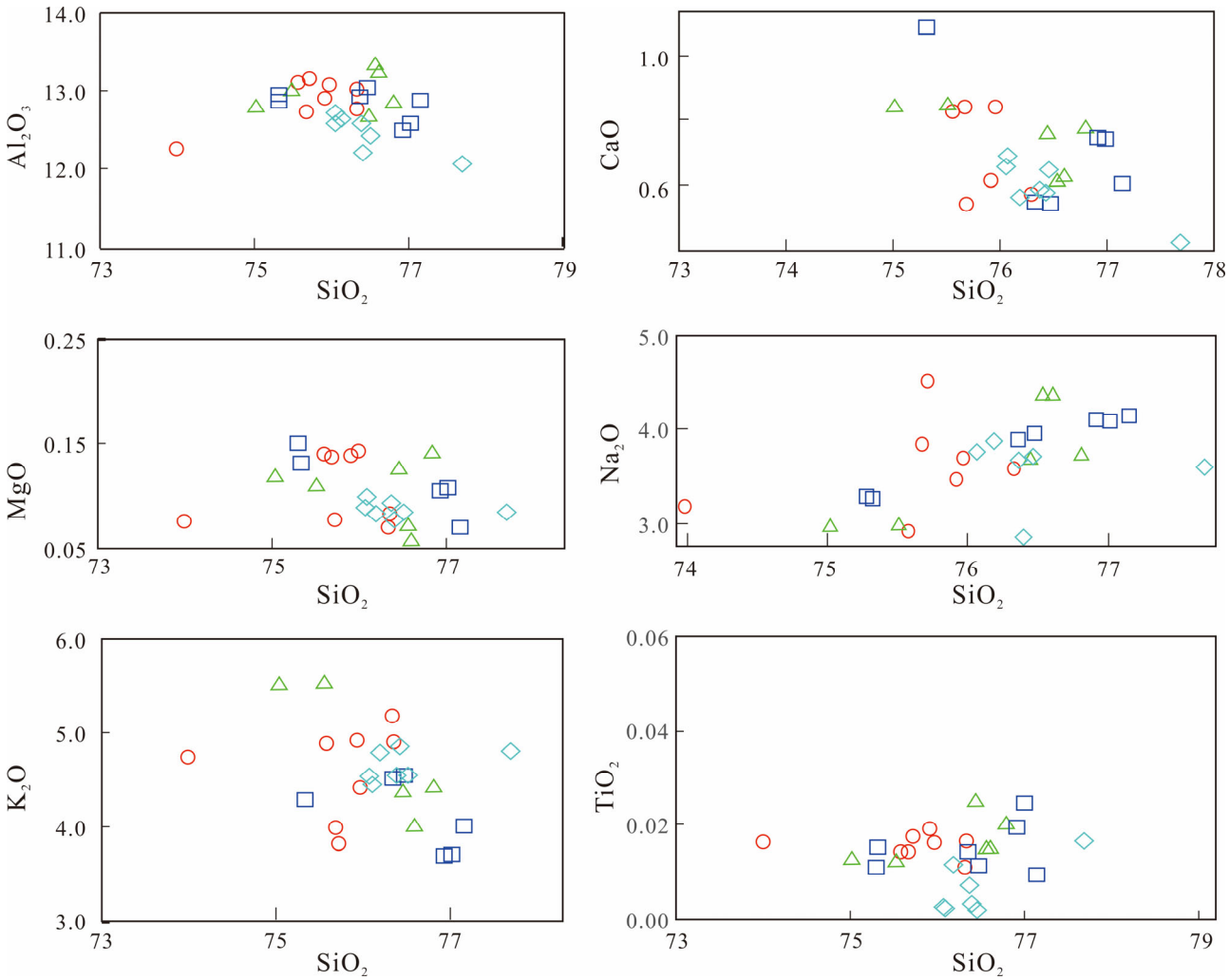


Figure 5. Harker diagrams for the Helong granites. Symbols as in Figure 4.

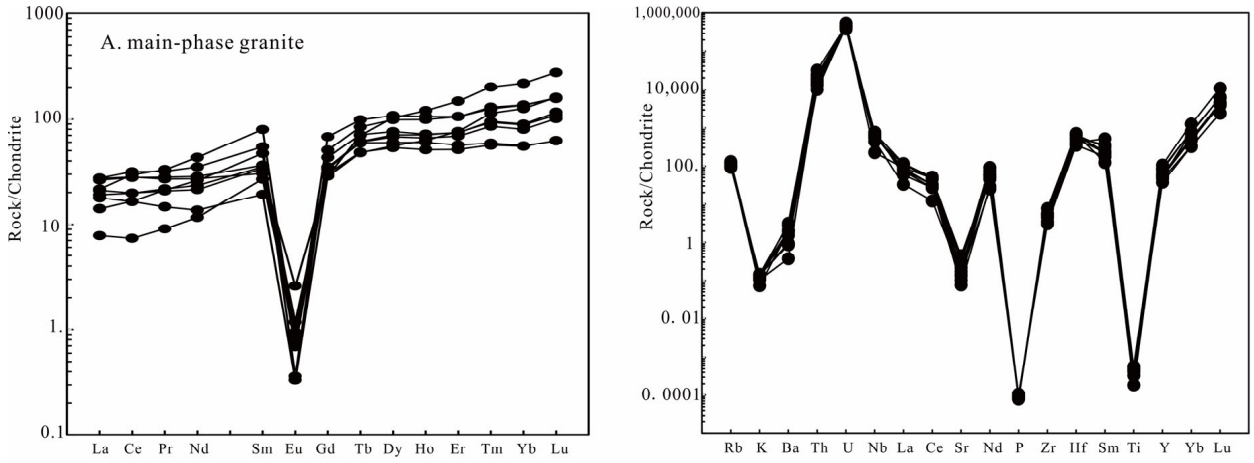


Figure 6. *Cont.*

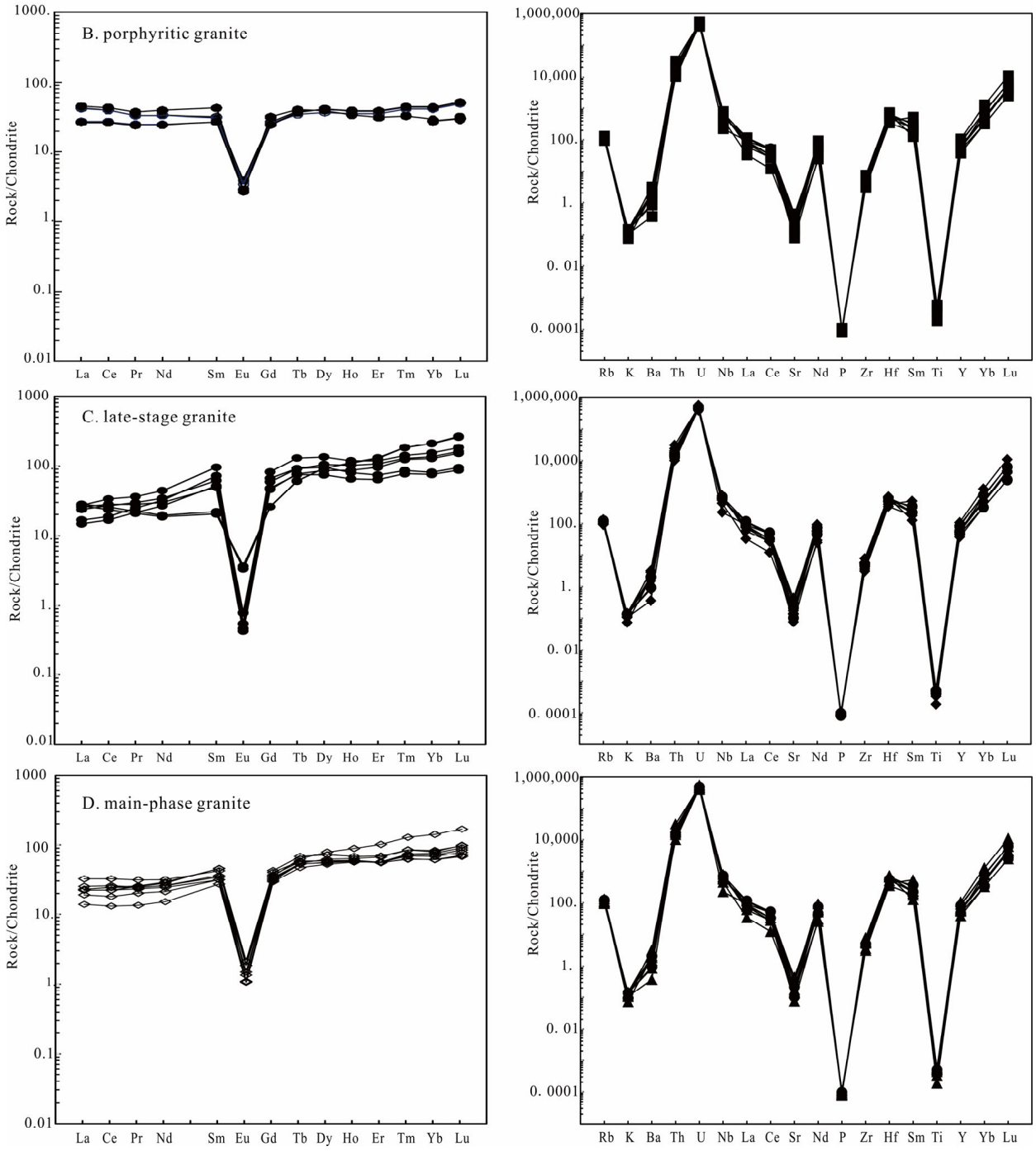


Figure 6. Chondrite-normalized REE patterns and element diagrams for the Jinzhuping granites (**A**–**C**), and the Changkeng granite (**D**). Normalization values are from Sun and McDonough [50].

4.2. LA-ICP-MS Zircon U–Pb Ages

Most of the zircon crystals selected from samples of JZP-6, JZP-12, and JZP-33 are short columnar, euhedral to subhedral, 60–180 μm long, and yield length/width ratios from 1:1 to 4:1. Most zircons are euhedral to subhedral, have well-developed oscillatory cathodoluminescence (CL) zoning (Figure 7), and are colorless to dark (most of samples JZP-6 and JZP-12) to dark and opaque (most of sample JZP-33). The age for each sample is given as the error-weighted mean of the common Pb-corrected $^{206}Pb/^{238}Pb$ ages of the selected grains at the 95% confidence level. The LA-ICP-MS U–Pb zircon geochronology

results for two dated samples are presented in Table 2, and U–Pb concordia diagrams are given in Figure 8.

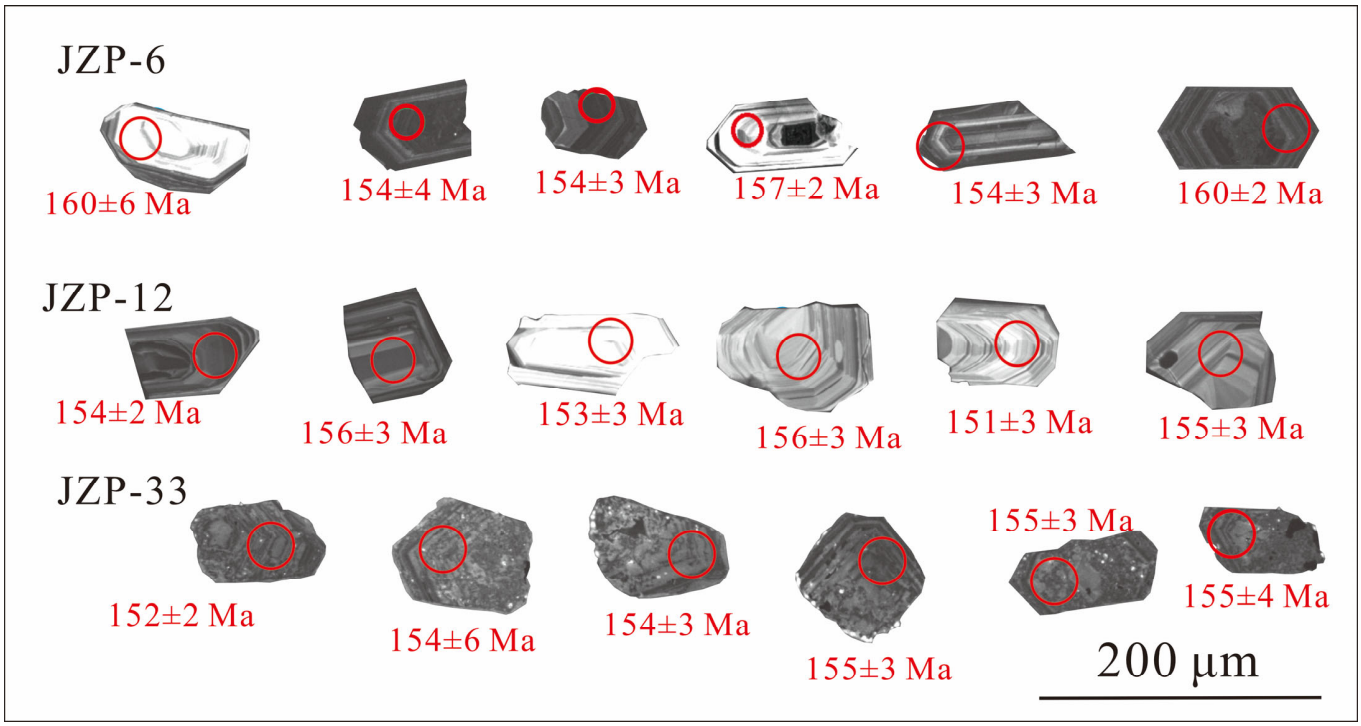


Figure 7. Cathodoluminescence (CL) images of zircon crystals from the Jinzhuping pluton.

Twenty-two zircon grains from sample JZP-6 were examined, and their U and Th concentrations varied from 118.2 to 20583.2 ppm (mean 3985.5 ppm) and from 66.5 to 1801.3 ppm (736.3 ppm), respectively, and the U/Th ratios varied from 1.1 to 10.8 (Table 2). These characteristics indicate a magmatic origin for the zircon grains. Sixteen spots of the zircon grains (from JZP-6-6 to JZP-6-22) were used, because the other six analyses yielded very high-U contents that would result in inaccurate U–Pb age calibrations [51]. These analyses yielded a concordant age of 155.2 ± 0.68 Ma (MSWD = 0.8) (Figure 8A), which coincided well with the weighted mean $^{206}Pb/^{238}U$ age of 155.5 ± 1.3 Ma (MSWD = 0.96) (Figure 8B). This age represents the crystallization age of the main-phase biotite granite.

Twenty-two zircon grains from sample JZP-12 were examined, and their U and Th concentrations varied from 80.6 to 482.9 ppm (mean 246.1 ppm) and from 54.4 to 318.6 ppm (154.6 ppm), respectively, and the U/Th ratios varied from 0.9 to 2.4 (Table 2). These characteristics indicate a magmatic origin for the zircons. These analyses yielded a concordant age of 154.0 ± 0.56 Ma (MSWD = 4.3) (Figure 8C), which coincided well with the weighted mean $^{206}Pb/^{238}U$ age of 153.8 ± 1.1 Ma (MSWD = 0.6) (Figure 8D). This age represents the crystallization age of the porphyritic biotite granite.

Zircons from the fine-grained granite (JZP-33) typically have rugged surfaces, contain microfractures, and are characterized by strikingly high U (2954.8–35794.6 ppm) and Th (152.4–4008.8 ppm), with U/Th = 6.8–68.4 (Table 2). The high U and Th contents indicate that zircons of JZP-33 were magmatic in origin, but suffered metamictization after crystallization. Seventeen spots were selected for analysis (from JZP-33-17 to JZP-33-30), and most of them showed discordant ages due to the metamictization of zircons. The 17 discordant spots yielded a lower intercept age of 153.4 ± 0.99 Ma (MSWD = 0.43) (Figure 8E), which coincided well with the weighted mean $^{206}Pb/^{238}U$ age of 154.6 ± 1.3 Ma (MSWD = 0.27) (Figure 8F). This age represents the upper limit of the crystallization age.

Table 2. LA-ICP-MS zircon U–Pb dating results of the Jinzhuping granites.

Sample Name	^{238}U μg/g	^{232}Th μg/g	$^{238}U/^{232}Th$	$^{207}Pb/^{206}Pb$	1sigma	$^{207}Pb/^{235}U$	1sigma	$^{206}Pb/^{238}U$	1sigma	$^{208}Pb/^{232}Th$	1sigma	$^{207}Pb/Pb206$ Age (Ma)	1sigma	$^{207}Pb/^{235}U$ Age (Ma)	1sigma	$^{206}Pb/^{238}U$ Age (Ma)	1sigma	$^{208}Pb/^{232}Th$ Age (Ma)	1sigma
Main-phase granite																			
JZP-6-1	673	257	2.7002	0.0931	0.0026	0.321	0.0081	0.0251	0.0003	0.0166	0.0005	1490	28	283	6	160	2	332	10
JZP-6-2	7718	1801	4.1953	0.0634	0.0014	0.2208	0.0086	0.0248	0.0006	0.0139	0.001	722	45	203	7	158	4	279	19
JZP-6-3	6097	823	4.0391	0.0604	0.001	0.209	0.0076	0.0252	0.001	0.012	0.0005	618	38	193	6	160	6	241	10
JZP-6-4	5591	1627	3.4859	0.0589	0.0028	0.2005	0.009	0.0247	0.0004	0.0076	0.0001	563	108	186	8	157	3	154	3
JZP-6-5	7178	1573	5.1905	0.0542	0.0026	0.1781	0.0082	0.0238	0.0003	0.0074	0.0001	381	111	166	7	152	2	150	2
JZP-6-6	5241	901	5.8981	0.0527	0.0009	0.1802	0.0035	0.0247	0.0003	0.0097	0.0003	317	21	168	3	157	2	194	7
JZP-6-7	20,583	1654	10.8275	0.0494	0.002	0.1625	0.0059	0.0238	0.0004	0.0075	0.0001	169	92	153	5	152	2	152	3
JZP-6-8	293	238	1.2983	0.0488	0.0015	0.1607	0.0049	0.024	0.0004	0.0082	0.0003	140	40	151	4	153	3	165	6
JZP-6-9	353	335	1.1247	0.0519	0.0021	0.1726	0.0078	0.0241	0.0006	0.0083	0.0002	281	62	162	7	154	3	167	5
JZP-6-10	7375	886	8.6269	0.0505	0.0021	0.1679	0.006	0.0241	0.0005	0.0076	0.0001	218	96	158	5	154	3	153	3
JZP-6-11	315	217	1.4828	0.0504	0.0027	0.169	0.0094	0.0242	0.0006	0.0087	0.0003	215	86	159	8	154	4	176	7
JZP-6-12	5164	1109	4.6679	0.0499	0.002	0.1663	0.0057	0.0242	0.0005	0.0076	0.0001	190	94	156	5	154	3	154	3
JZP-6-13	172	94	1.8037	0.0498	0.0017	0.1643	0.0057	0.0242	0.0004	0.0075	0.0003	186	52	154	5	154	2	152	6
JZP-6-14	118	76	1.638	0.0495	0.0031	0.1617	0.0093	0.0242	0.0005	0.0081	0.0004	170	96	152	8	154	3	164	8
JZP-6-15	231	132	1.8046	0.049	0.0018	0.1637	0.0062	0.0242	0.0004	0.0085	0.0004	149	56	154	5	154	3	172	9
JZP-6-16	7831	1346	5.9222	0.0482	0.0017	0.1611	0.0047	0.0242	0.0005	0.0077	0.0001	111	80	152	4	154	3	155	3
JZP-6-17	3589	470	7.9002	0.0505	0.0024	0.1712	0.0074	0.0246	0.0004	0.0078	0.0002	219	110	160	6	157	3	156	4
JZP-6-18	394	173	2.3204	0.0494	0.0016	0.1673	0.0052	0.0247	0.0004	0.0081	0.0003	166	46	157	5	157	2	164	6
JZP-6-19	5691	702	8.2496	0.0496	0.0013	0.1698	0.0037	0.0248	0.0004	0.0079	0.0001	174	64	159	3	158	2	158	2
JZP-6-20	135	66	2.1132	0.0489	0.0026	0.1679	0.0092	0.0249	0.0005	0.0079	0.0004	144	87	158	8	158	3	159	8
JZP-6-21	2644	1604	1.9477	0.0482	0.0037	0.1652	0.0114	0.0248	0.0008	0.0079	0.0002	110	172	155	10	158	5	159	4
JZP-6-22	293	113	2.7514	0.0504	0.0018	0.1738	0.0061	0.0251	0.0004	0.0089	0.0005	213	54	163	5	160	2	179	10
Porphyritic granite																			
JZP-12-1	423	277	1.5273	0.05	0.0013	0.1663	0.005	0.024	0.0004	0.0075	0.0002	197	61	156	4	153	2	150	4
JZP-12-2	83	54	1.5301	0.0492	0.003	0.1646	0.01	0.0246	0.0005	0.0074	0.0004	156	142	155	9	156	3	150	8
JZP-12-3	151	123	1.2233	0.0494	0.0022	0.1619	0.0071	0.0239	0.0004	0.0074	0.0003	167	105	152	6	152	2	150	7
JZP-12-4	203	88	2.3013	0.0501	0.0019	0.1688	0.0066	0.0245	0.0003	0.0087	0.0004	198	90	158	6	156	2	175	7
JZP-12-5	113	64	1.7532	0.0513	0.0022	0.1682	0.0072	0.0241	0.0005	0.0076	0.0005	254	99	158	6	153	3	154	11
JZP-12-6	190	96	1.981	0.0503	0.0019	0.1653	0.0062	0.024	0.0004	0.0082	0.0004	208	86	155	5	153	2	164	8
JZP-12-7	110	56	1.964	0.0518	0.0028	0.1733	0.0084	0.0246	0.0005	0.0076	0.0005	276	125	162	7	156	3	153	10
JZP-12-8	81	65	1.2427	0.05	0.0025	0.1605	0.0078	0.0237	0.0005	0.0078	0.0004	196	115	151	7	151	3	157	8
JZP-12-9	227	183	1.2426	0.0511	0.0023	0.1691	0.0074	0.0242	0.0006	0.0076	0.0005	243	105	159	6	154	4	153	10
JZP-12-10	291	123	2.3643	0.0503	0.0021	0.169	0.0068	0.0244	0.0003	0.0079	0.0003	207	98	159	6	156	2	159	7
JZP-12-11	118	67	1.7685	0.05	0.0022	0.1654	0.0069	0.0242	0.0004	0.0082	0.0006	194	101	155	6	154	3	165	11
JZP-12-12	311	192	1.6235	0.0503	0.0018	0.1672	0.0059	0.0241	0.0004	0.0083	0.0003	207	82	157	5	154	3	168	5
JZP-12-13	152	116	1.3038	0.0489	0.0024	0.1659	0.0083	0.0246	0.0004	0.0074	0.0005	142	113	156	7	157	3	149	11
JZP-12-14	140	97	1.4428	0.0511	0.0025	0.1703	0.0085	0.0243	0.0005	0.0078	0.0004	246	114	160	7	155	3	157	8
JZP-12-15	750	434	1.7304	0.0494	0.001	0.1622	0.004	0.0238	0.0003	0.0075	0.0003	169	50	153	3	152	2	151	5
JZP-12-16	104	101	1.0325	0.0503	0.0032	0.1618	0.0107	0.0236	0.0005	0.0071	0.0004	210	149	152	9	151	3	144	9
JZP-12-17	293	148	1.9804	0.0513	0.0016	0.1723	0.0057	0.0244	0.0004	0.0076	0.0003	253	74	161	5	155	3	153	6
JZP-12-18	483	295	1.639	0.0507	0.0012	0.1654	0.0042	0.0238	0.0003	0.0071	0.0003	226	53	155	4	151	2	143	5
JZP-12-19	414	319	1.2999	0.0488	0.0014	0.1651	0.0051	0.0246	0.0004	0.0075	0.0002	136	67	155	4	157	3	151	5
JZP-12-20	356	158	2.2604	0.0496	0.0025	0.1616	0.0076	0.0238	0.0006	0.0074	0.0004	175	118	152	7	152	4	149	8
JZP-12-21	182	215	0.847	0.05	0.0019	0.167	0.0069	0.0246	0.0005	0.0078	0.0003	196	89	157	6	157	3	156	6
JZP-12-22	239	131	1.8196	0.0503	0.0022	0.1637	0.007	0.0237	0.0004	0.0079	0.0005	208	101	154	6	151	3	160	10

Table 2. *Cont.*

Sample Name	^{238}U μg/g	^{232}Th μg/g	$^{238}U/^{232}Th$	$^{207}Pb/^{206}Pb$	1sigma	$^{207}Pb/^{235}U$	1sigma	$^{206}Pb/^{238}U$	1sigma	$^{208}Pb/^{232}Th$	1sigma	$^{207}Pb/Pb206$ Age (Ma)	1sigma	$^{207}Pb/^{235}U$ Age (Ma)	1sigma	$^{206}Pb/^{238}U$ Age (Ma)	1sigma	$^{208}Pb/^{232}Th$ Age (Ma)	1sigma
										Aplite									
JZP-33-1	3926	255	15.4011	0.0544	0.002	0.1793	0.0062	0.0239	0.0003	0.0075	0.0002	387	85	167	5	152	2	150	4
JZP-33-2	11,616	905	12.8339	0.0527	0.0028	0.1779	0.0072	0.0245	0.0009	0.0077	0.0003	317	124	166	6	156	5	154	5
JZP-33-3	4525	235	19.2307	0.0525	0.0038	0.17	0.0111	0.0235	0.0007	0.0074	0.0004	307	165	159	10	150	4	148	7
JZP-33-4	5364	489	10.9679	0.0525	0.0007	0.1753	0.0025	0.0241	0.0003	0.0066	0.0003	308	14	164	2	154	2	134	6
JZP-33-5	5856	338	17.3319	0.0587	0.0033	0.1911	0.0102	0.0236	0.0005	0.0073	0.0003	556	127	178	9	150	3	147	5
JZP-33-6	4296	427	10.052	0.0559	0.0013	0.1874	0.0037	0.0243	0.0002	0.0076	0.0001	447	51	174	3	155	2	153	2
JZP-33-7	5927	877	6.7598	0.055	0.0035	0.18	0.0107	0.0237	0.0005	0.0074	0.0002	412	145	168	9	151	3	149	3
JZP-33-8	8268	931	8.8796	0.0548	0.0046	0.1828	0.0137	0.0242	0.0009	0.0076	0.0003	404	191	170	12	154	6	152	5
JZP-33-9	16,324	806	20.2414	0.0527	0.0006	0.1773	0.0056	0.0245	0.0008	0.0142	0.0006	315	33	166	5	156	5	285	11
JZP-33-10	31,531	3344	9.4285	0.0537	0.0012	0.1805	0.0047	0.0246	0.0006	0.0128	0.0006	357	27	168	4	156	4	257	11
JZP-33-11	3897	497	7.8437	0.0565	0.0035	0.1877	0.0112	0.0241	0.0004	0.0075	0.0003	471	142	175	10	154	3	151	5
JZP-33-12	15,528	1627	9.5436	0.0519	0.0022	0.1748	0.0061	0.0244	0.0006	0.0077	0.0002	280	99	164	5	156	4	155	4
JZP-33-13	8352	632	13.2072	0.0533	0.0019	0.1773	0.0055	0.0241	0.0004	0.0076	0.0002	343	83	166	5	154	3	152	3
JZP-33-14	11,340	713	15.916	0.0506	0.0014	0.1688	0.0035	0.0242	0.0004	0.0076	0.0002	221	64	158	3	154	3	154	3
JZP-33-15	5043	406	12.4223	0.0509	0.0006	0.172	0.0037	0.0244	0.0005	0.007	0.0004	234	22	161	3	155	3	140	8
JZP-33-16	7647	492	15.5315	0.0502	0.0026	0.1683	0.0079	0.0243	0.0005	0.0077	0.0003	205	121	158	7	155	3	154	5
JZP-33-17	4391	249	17.6263	0.0495	0.0014	0.1657	0.0035	0.0243	0.0004	0.0077	0.0001	171	65	156	3	155	3	155	3
JZP-33-18	4715	479	9.8434	0.0513	0.0025	0.1735	0.0067	0.0245	0.0007	0.0077	0.0002	254	116	162	6	156	5	155	5
JZP-33-19	4496	210	21.4366	0.0506	0.0018	0.1711	0.005	0.0246	0.0005	0.0077	0.0002	220	86	160	4	156	3	156	4
JZP-33-20	5662	282	20.055	0.0513	0.002	0.1708	0.0053	0.0241	0.0006	0.0076	0.0002	255	93	160	5	154	4	153	4
JZP-33-21	3820	152	25.0591	0.051	0.0018	0.1693	0.0054	0.0241	0.0004	0.0076	0.0002	239	84	159	5	153	2	153	4
JZP-33-22	16,291	1343	12.1274	0.0506	0.0022	0.1719	0.0056	0.0246	0.0007	0.0078	0.0002	225	102	161	5	157	4	156	4
JZP-33-23	30,986	4009	7.7295	0.0513	0.0006	0.1739	0.0037	0.0245	0.0005	0.0058	0.0003	255	22	163	3	156	3	118	7
JZP-33-24	8695	696	12.4978	0.0508	0.0012	0.1714	0.0033	0.0245	0.0004	0.0077	0.0001	233	57	161	3	156	2	155	2
JZP-33-25	35,795	523	68.4089	0.0508	0.0006	0.1683	0.0041	0.0244	0.0006	0.0155	0.001	232	27	158	4	156	4	311	19
JZP-33-26	4079	224	18.232	0.0516	0.0021	0.1745	0.006	0.0245	0.0005	0.0077	0.0002	266	96	163	5	156	3	155	5
JZP-33-27	4586	313	14.6707	0.0512	0.0015	0.1701	0.0042	0.0241	0.0003	0.0076	0.0002	249	67	160	4	154	2	153	3
JZP-33-28	2955	282	10.4913	0.049	0.0031	0.1639	0.0095	0.0243	0.0006	0.0077	0.0003	146	143	154	8	155	4	155	6
JZP-33-29	7740	456	16.9802	0.0509	0.0014	0.1675	0.004	0.0239	0.0004	0.0075	0.0001	236	67	157	3	152	2	151	2
JZP-33-30	19,129	1464	13.0672	0.0508	0.0016	0.1701	0.0045	0.0243	0.0004	0.0077	0.0001	231	73	159	4	155	2	154	3

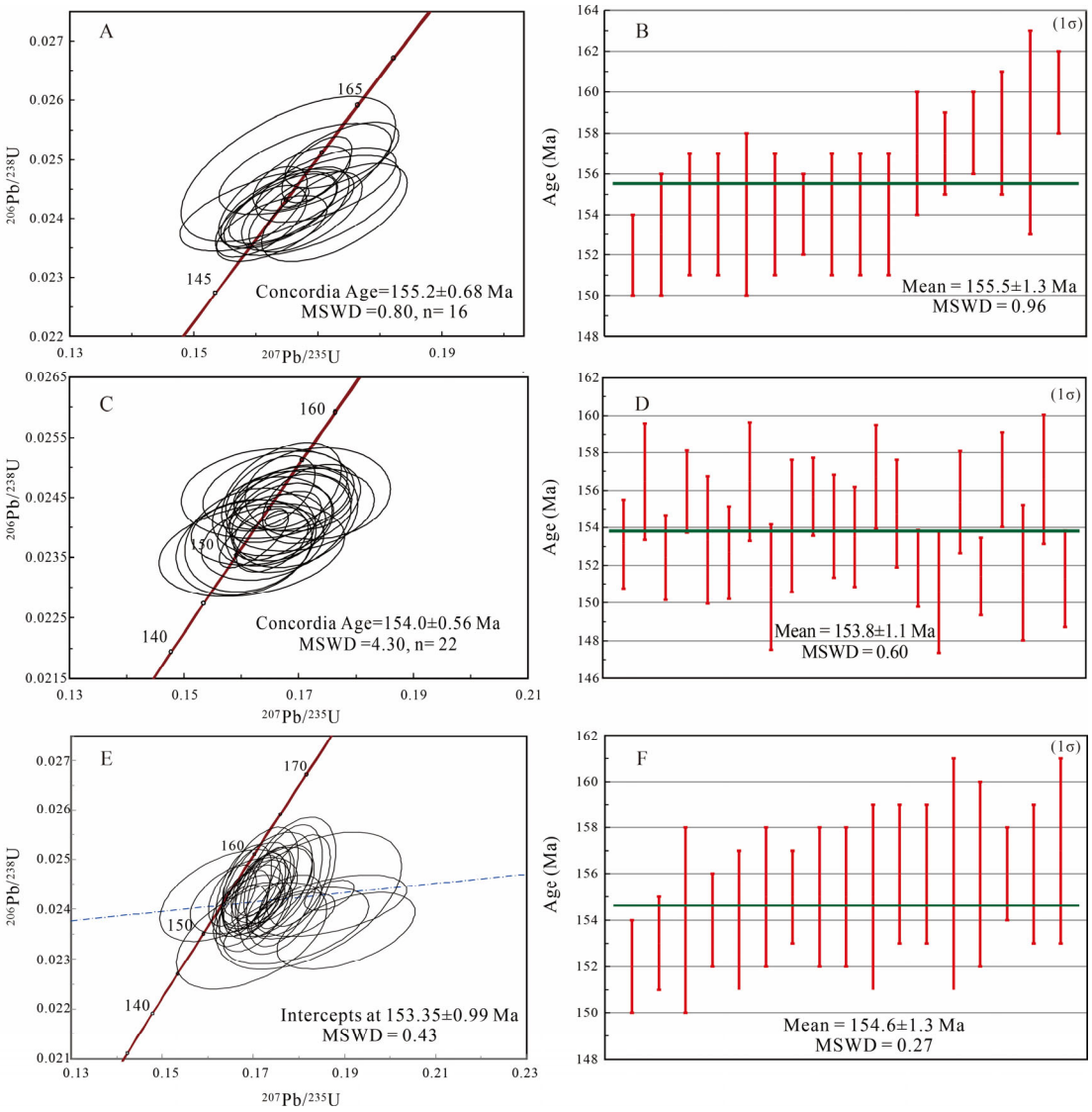


Figure 8. LA-ICP-MS U–Pb concordia diagrams and weighted mean $^{206}Pb/^{238}U$ ages of zircon in the Jinzhuping medium to coarse-grained biotite granite (**A**,**B**), porphyritic biotite granite (**C**,**D**) and aplite (**E**,**F**).

4.3. Zircon Hf Isotopes

The zircon Hf isotope determination points were the same sites as the zircon U–Pb measurements. The data from the fifty measured spots of the Jinzhuping granite samples are shown in Table 3 and plotted on Figure 9. The Hf isotopic analyses for 15 zircon grains from the main-phase biotite granite (sample JZP-6), with initial $^{176}Hf/^{177}Hf$ ratios varying from 0.282292 to 0.282406, yield $\varepsilon_{Hf}(t)$ values from −14.2 to −10.4. The Hf isotopic analyses for 18 zircon grains from the porphyritic biotite granite (sample JZP-12), with initial $^{176}Hf/^{177}Hf$ ratios varying from 0.282257 to 0.282370, yield $\varepsilon_{Hf}(t)$ values from −15.3 to −11.4. There are 17 spots for the aplite (Sample JZP-33), providing initial $^{176}Hf/^{177}Hf$ ratios of 0.282190−0.282410, corresponding to an $\varepsilon_{Hf}(t)$ from −18.1 to −10.5. Their two-stage Hf model ages (T_{DM2}) range from 1.83 to 2.06 Ga, from 1.89 to 2.14 Ga, and from 1.83 to 2.31 Ga, respectively.

Table 3. In situ zircon Hf isotopic results of the Helong granites.

Sample	t(Ma)	$^{176}Yb/^{177}Hf$(corr)	2σ	$^{176}Lu/^{177}Hf$(corr)	2σ	$^{176}Hf/^{177}Hf$(corr)	2σ	εHf(t)	Error	T_{DM} (Ma)	T_{2DM} (Ma)
JK-6-001	153.6	0.051877	0.000462	0.001488	0.000018	0.282300	0.000016	−13.9	0.6	1361	2046
JK-6-002	157.2	0.037588	0.000574	0.001098	0.000016	0.282342	0.000017	−12.3	0.6	1289	1950
JK-6-003	154	0.069477	0.002347	0.001840	0.000051	0.282323	0.000021	−13.1	0.7	1342	1998
JK-6-004	158.7	0.067714	0.001052	0.002059	0.000029	0.282343	0.000015	−12.3	0.5	1320	1951
JK-6-005	154.7	0.128123	0.004076	0.003860	0.000060	0.282406	0.000015	−10.4	0.5	1293	1827
JK-6-006	152.6	0.048225	0.000812	0.001366	0.000020	0.282349	0.000027	−12.2	1.0	1287	1937
JK-6-007	153.8	0.053523	0.002942	0.001388	0.000073	0.282292	0.000021	−14.2	0.7	1369	2063
JK-6-008	159.3	0.367416	0.011419	0.009588	0.000293	0.282368	0.000024	−12.2	0.8	1616	1947
JK-6-009	154.3	0.057902	0.000735	0.001611	0.000027	0.282371	0.000016	−11.4	0.6	1264	1889
JK-6-010	153.8	0.026043	0.000379	0.000700	0.000006	0.282314	0.000016	−13.3	0.6	1314	2011
JK-6-011	161.3	0.198931	0.013431	0.004777	0.000297	0.282332	0.000015	−13.0	0.5	1443	1993
JK-6-012	159.7	0.044705	0.001973	0.001197	0.000054	0.282304	0.000018	−13.6	0.6	1344	2031
JK-6-013	155.1	0.020640	0.000135	0.000586	0.000005	0.282311	0.000015	−13.4	0.5	1314	2016
JK-6-014	155	0.098174	0.002005	0.002940	0.000044	0.282308	0.000017	−13.7	0.6	1405	2038
JK-6-015	153.8	0.148483	0.004720	0.004274	0.000103	0.282391	0.000015	−11.0	0.5	1332	1863
JK-12-001	153.1	0.072649	0.000867	0.002016	0.000014	0.282367	0.000017	−11.6	0.6	1285	1903
JK-12-002	156.5	0.026296	0.001065	0.000760	0.000023	0.282303	0.000017	−13.6	0.6	1330	2032
JK-12-003	152.4	0.028996	0.000611	0.000787	0.000014	0.282297	0.000019	−14.0	0.7	1340	2049
JK-12-004	155.9	0.033672	0.000396	0.001021	0.000016	0.282362	0.000017	−11.6	0.6	1258	1906
JK-12-005	153.4	0.032392	0.000827	0.000907	0.000029	0.282293	0.000016	−14.1	0.6	1350	2057
JK-12-006	152.7	0.025960	0.000219	0.000754	0.000009	0.282337	0.000019	−12.5	0.7	1284	1961
JK-12-007	156.5	0.031122	0.000158	0.000906	0.000009	0.282275	0.000017	−14.7	0.6	1375	2096
JK-12-008	150.9	0.027296	0.000724	0.000815	0.000028	0.282370	0.000019	−11.4	0.7	1240	1889
JK-12-009	156.5	0.026885	0.000188	0.000762	0.000003	0.282314	0.000016	−13.2	0.6	1315	2008
JK-12-010	154.1	0.028758	0.000093	0.000830	0.000007	0.282338	0.000016	−12.5	0.6	1285	1959
JK-12-011	153.5	0.030214	0.001068	0.000860	0.000026	0.282325	0.000014	−13.0	0.5	1304	1988
JK-12-012	156.7	0.037258	0.000634	0.001059	0.000025	0.282319	0.000016	−13.1	0.6	1319	2000
JK-12-013	154.8	0.033840	0.000763	0.000926	0.000014	0.282257	0.000017	−15.3	0.6	1401	2137
JK-12-014	151.8	0.032556	0.000290	0.000938	0.000007	0.282307	0.000015	−13.6	0.5	1332	2029
JK-12-015	150.7	0.034999	0.000446	0.001006	0.000006	0.282323	0.000017	−13.1	0.6	1311	1994
JK-12-016	155.4	0.036607	0.000353	0.001040	0.000004	0.282289	0.000017	−14.2	0.6	1361	2067
JK-12-017	151.4	0.050925	0.002397	0.001573	0.000080	0.282316	0.000015	−13.4	0.5	1341	2012
JK-12-018	156.7	0.043864	0.000743	0.001253	0.000015	0.282309	0.000018	−13.5	0.6	1341	2024

Table 3. *Cont.*

Sample	t(Ma)	$^{176}Yb/^{177}Hf$(corr)	2σ	$^{176}Lu/^{177}Hf$(corr)	2σ	$^{176}Hf/^{177}Hf$(corr)	2σ	εHf(t)	Error	T_{DM} (Ma)	T_{2DM} (Ma)
JK-33-001	158.2	0.049946	0.001058	0.001496	0.000041	0.282313	0.000008	−13.3	0.3	1343	2015
JK-33-002	106.9	0.109099	0.003831	0.003074	0.000070	0.282348	0.000010	−13.3	0.4	1350	1973
JK-33-003	155.3	0.414276	0.007500	0.011005	0.000145	0.282374	0.000028	−12.2	1.0	1687	1944
JK-33-004	157	0.091055	0.003138	0.002697	0.000075	0.282337	0.000013	−12.7	0.4	1353	1971
JK-33-005	155.5	0.050148	0.000754	0.001491	0.000023	0.282328	0.000012	−12.9	0.4	1321	1983
JK-33-006	155.7	0.167892	0.003711	0.004775	0.000094	0.282369	0.000012	−11.7	0.4	1385	1913
JK-33-007	152.9	0.182933	0.003573	0.004888	0.000073	0.282190	0.000145	−18.1	5.1	1668	2310
JK-33-008	155.9	0.231805	0.012291	0.006460	0.000301	0.282410	0.000019	−10.5	0.7	1391	1835
JK-33-009	156.4	0.066568	0.002530	0.001897	0.000074	0.282359	0.000014	−11.8	0.5	1291	1916
JK-33-010	156	0.408961	0.011939	0.010215	0.000270	0.282404	0.000021	−11.0	0.8	1583	1870
JK-33-011	155.5	0.088331	0.001185	0.002404	0.000021	0.282301	0.000014	−13.9	0.5	1394	2049
JK-33-012	158.4	0.232678	0.008136	0.006027	0.000204	0.282377	0.000019	−11.6	0.7	1426	1904
JK-33-013	158.7	0.135885	0.001637	0.003855	0.000042	0.282318	0.000018	−13.4	0.6	1426	2019
JK-33-014	155	0.026320	0.001176	0.000694	0.000032	0.282320	0.000012	−13.1	0.4	1305	1996
JK-33-015	157.6	0.077232	0.002839	0.002053	0.000066	0.282365	0.000015	−11.6	0.5	1288	1903
JK-33-016	156.9	0.080254	0.001098	0.002269	0.000027	0.282337	0.000013	−12.6	0.5	1337	1968
JK-33-017	155.2	0.088109	0.003025	0.002287	0.000071	0.282346	0.000015	−12.3	0.5	1324	1949

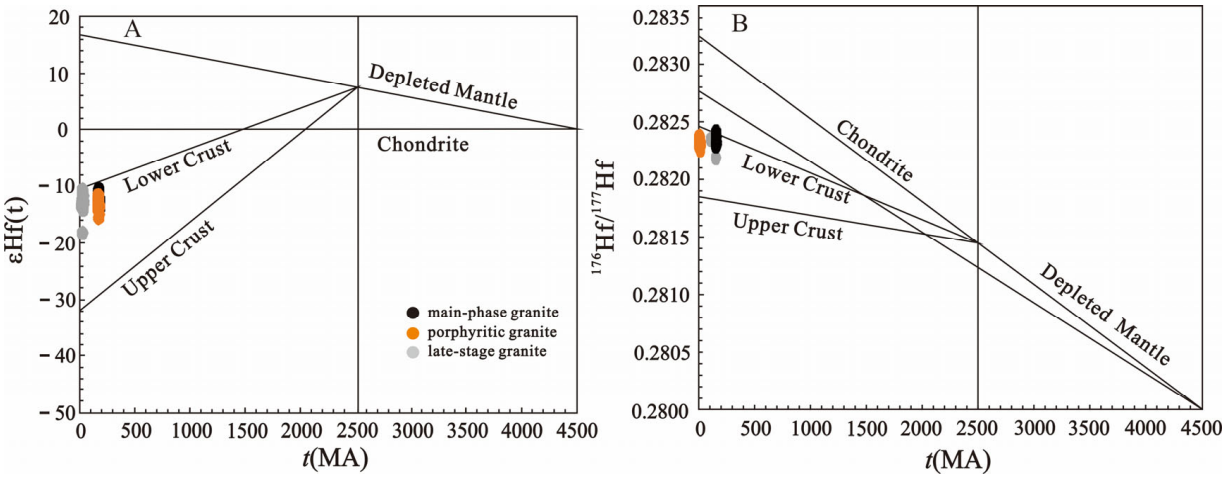


Figure 9. εHf(t) vs. age plots (**A**) and $^{176}Hf/^{177}Hf$ vs. age plots (**B**) for the Jinzhuping zircons.

5. Discussion

5.1. Geochronology of the Helong Granites

The "high-U effect" of zircon grains has been known for many years, and may lead to uncertainties in age results and greater discordance in the concordia diagram than normal zircons using the U–Pb method [52–54]. It is likely to be caused by radiogenic damage to the crystal lattice and subsequent alteration of zircon grains [55]. Many works have been done on the metamict effect of zircon grains with high U and Th. The physical properties of zircon grains, such as an increase in solubility and becoming opaque, could be affected by radioactive damage [56,57]. The "high-U effect" attributed to enhanced ionization of Pb results in a positive correlation between the apparent ages and the U or U/Th contents of zircon grains [54,58,59], but not all high-U zircon grains yield anomalously old U–Pb dates [60], in some cases the positive correlation may be slight or in existence [54].

More than half of zircon grains from the Jinzhuping main-phase granite have high uranium and thorium concentrations (more than 2500 μg/g and 1100 μg/g) that may lead to uncertainties in age. All the grains show no correlation between U and apparent age. Except for some zircon grains with high-U contents that have weakly older ages (ca. 160 Ma), the other grains show very close ages (ca.152–158 Ma), and yield a well weighted mean $^{206}Pb/^{238}U$ age (155.5 ± 1.3 Ma) (Figure 8B). Therefore, the main-phase granite of the Jinzhuping pluton was crystallized at ca. 152 to 160 Ma. The porphyritic biotite granite, formed by the structural change of the main-phase granite, has low uranium and thorium concentrations, and then their close ages of zircon grains from ca. 151 to 157 Ma present their crystallization ages. Zircon grains from the late-stage Jinzhuping aplite are characterized by high uranium and thorium concentrations, but there is no correlation between U and apparent age. Most of the zircon crystals are altered by hydrotherm (as shown in Figure 7), and thus, the lower intercept age of 153.4 ± 0.99 Ma should be the upper limit of the crystallization age. The 17 discordant spots used to yield weighted mean age for the aplite show an age range from ca. 150 Ma to 157 Ma, and are considered to be the age of hydrothermal activities after the emplacement of this igneous rock.

Previously published age data for the Helong granites have been zircon U–Pb isotope ages, which are ca. 159 Ma for the Jinzhuping porphyritic biotite granite and ca. 157 Ma for the Changkeng biotite granite [29,31]. In our study, precise LA-ICP-MS zircon U–Pb dates, within the error, obtained for the main-phase biotite granite, porphyritic biotite granite, and the aplite of the Jinzhuping deposit, are consistent, suggesting that the Helong granites were emplaced within a very short period, i.e., from ca. 150 Ma to 159 Ma.

5.2. Granite Sources

According to the studies of Sylvester [61], peraluminous granite formed by partial melting of source materials with different compositions will result in different CaO/Na_2O ratios. The CaO/Na_2O ratio of granites formed from mudstone (<0.3) is lower than that of granites formed from clastic rocks. In the Rb/Sr-Rb/Ba diagram (Figure 10A), the Helong granites in southern Jiangxi Province mainly fall into the clay-rich source area, and in the Rb/Sr-CaO/Na_2O diagram (Figure 10B), they fall into the argillite source region. Su et al. [28] suggested that the granitoids related to W–Sn deposits in the southern Jiangxi Province mainly formed from argillaceous rock rich in clay. This conclusion also supports the interpretation that the Helong granites were derived from the fertile crustal source.

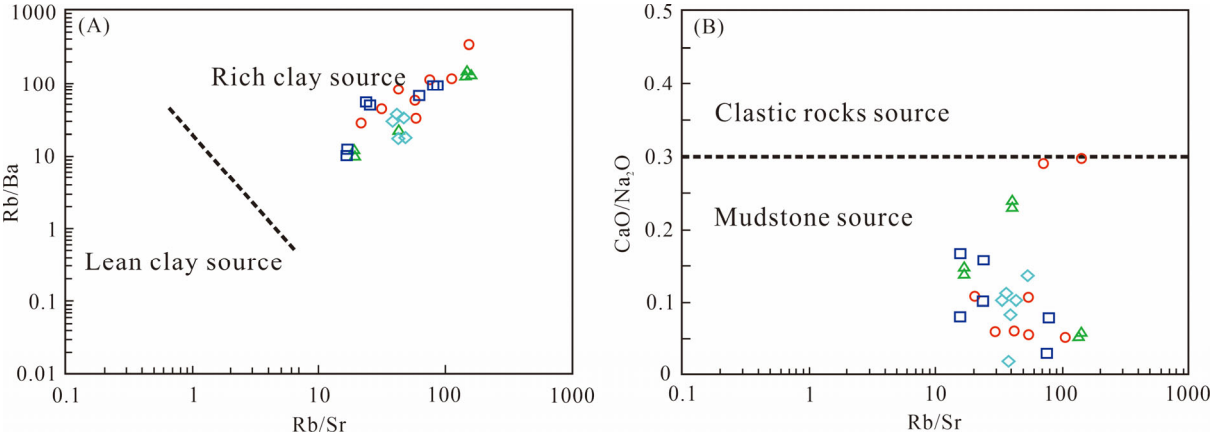


Figure 10. The Rb/Sr-Rb/Ba diagram (**A**) and the Rb/Sr-CaO/Na_2O diagram (**B**) of the Helong granites. Symbols as in Figure 4.

The variations of composition and the correlation of elements in Harker diagrams (Figure 5) indicate that the Helong granites probably derived from homogeneous sources. The $^{176}Hf/^{177}Hf$ values of the Jinzhuping granites fall around the line of the lower crust (Figure 9A,B), which is same with the Changkeng granite [29], indicating that the Helong magma was derived from the lower crust. Hf two-stage model T_{DM} ages (1.83–2.31 Ga) indicate that the Jinzhuping granites may have resulted from the Paleoproterozoic crustal materials, which is consistent with the source of Changkeng granite [29]. Therefore, the Helong granites derived from partial melting of the Late Paleoproterozoic crustal materials. Low εHf(t) values from −18.1 to −10.1 with an average value of −12.8 for Jinzhuping granites, and from −14.1 to −11.1 with an average value of −12.9 for Changkeng granite [29] (Figure 9) indicate that possibly there was no involvement of mantle-derived materials.

5.3. Degrees of Fractional Crystallization of Helong Granites

The Helong granites are rich in Rb, Th, U, Nb, Ta, Nd, and Sm. Strong depletions in Eu, Ba, Sr, P, and Ti prove that crystallization of plagioclase, apatite, and Ti–Fe oxides occurred during their formation (Figure 6).

The Jinzhuping main-phase granite has the strongest depletions in Eu, P, Ti, and Sr in the four granites (Figure 6). The average Sr contents of Changkeng and Jinzuping granites (from the main-phase, porphyritic to aplite) increase from 11.1 to 11.2 to 15.9 to 17.5 μg/g. The average Ba contents of the four granites are 19.6, 10.1, 30.8, and 18.0 μg/g, respectively. The K/Rb ratio can reflect the degree of magma differentiation evolution, and a low K/Rb ratio is usually one of the important characteristics of highly evolved magmatic systems [62–64]. The K/Rb ratios of the Helong ore-hosting granites are all low, with average values of 84.15, 63.43, 60.76, and 64.84, respectively. The Zr/Hf ratio of rocks indicates the evolution degree of magmatic system and whether fluid metasomatism has occurred. The Zr/Hf ratio of granites decreases with increasing degree of evolution

or fluid metasomatism [62,63]. The average Zr/Hf ratios of the four granites are 13.14, 12.02, 15.05, and 11.28, respectively, which are significantly lower than those of ordinary granites (39) [28]. This result indicates that the Helong granites have undergone large-scale fluid metasomatism, in a similar way to what happened with granites from the granites in Southern Jiangxi Province [28]. On the basis of above evidences, the Helong granites experienced a high degree of differentiation and evolution, while the degree of the main-phase Jinzhuping granite is much higher than other granites.

5.4. Geodynamic Setting of the Helong Granites

There are close temporal, spatial, and genetic relationships between granitic rocks and intensive metallic mineralization in southern Jiangxi Province, Nanling Region in Mesozoic [2,4–6,29,65]. Research has shown that the Nanling area was in a lithospheric extensional environment in the early Yanshanian [35,65,66]. For example, Mao et al. [67] proposed that the magmatism and mineralization in East China dated at ca. 180–135 Ma formed within a continental magmatic arc, with widespread magmatism and back-arc extension caused by low-angle subduction of the Paleopacific plate. By comparing two sets of different metallogenic series and their related granites in Jurassic of Qinhang belt (Middle Jurassic porphyry-skarn-hydrothermal vein copper-gold polymetallic deposit and late Jurassic greisen-quartz vein-skarn W–Sn polymetallic deposit), Guo et al. [26] and Mao et al. [67] suggested that the large-scale diagenetic and metallogenic events in this belt were formed in the back-arc extensional environment related to the Pacific subduction.

Many Jurassic W–Sn granitic plutons including Helong, Baxiannao, Pangushan, Xihuashan, Taoxikeng, Jiulongnao, Baoshan, and Zhangdoukeng are located in the southern Jiangxi Province [5,9–11,13,29,68,69]. Su et al. [28] has recognized that, compositionally, these ore-hosting granites are high-K calc-alkaline; peraluminous; highly differentiated; enriched in Rb, U, and Th; depleted in Nd, Zr, Ti, Eu, Ba, Sr, and P; with low Al_2O_3, TiO_2, MgO, P_2O_5 values; and probably formed during lithospheric thinning and crustal extension. For example, Fang et al. [38,69] suggested that the Pangushan granite crystallized from high-K calc-alkaline, from metaluminous to peraluminous and highly differentiated magmas, and formed in an intraplate extension environment. Many researchers believe that the Nanling area was in a lithospheric extensional environment in the early Yanshanian [27,33,35,65,66,70]. In conclusion, few W–Sn-related granites including Jinzhuping and Changkeng in the Helong orefield occurred within an extensional environment caused by Paleopacific subduction in the middle to late Jurassic.

6. Conclusions

(1) The Helong granites include three different phases in the Jinzhuping ore deposit, i.e., main-phase biotite granite, porphyritic biotite granite, and aplite, as well as the Changkeng main-phase biotite granite.
(2) LA-ICP-MS zircon U–Pb ages confirm that the Jinzhuping granites were emplaced in the Late Jurassic. The ages of main-phase biotite granite, porphyritic biotite granite, and aplite are 155.2 ± 0.68 Ma, 154.0 ± 0.56 Ma, and 153.4 ± 0.99 Ma, respectively.
(3) Four granites were derived by partial melting of the Paleoproterozoic crustal materials, and they underwent high degrees of fractional crystallization.
(4) Helong granites hosting W–Sn deposits in the Nanling W–Sn polymetallic metallogenic belt occurred within a backarc setting with significant lithosphere thinning, probably caused by low-angle subduction of the Paleopacific plate.

Author Contributions: Conceptualisation, W.S. and J.Z.; field investigation, X.Z., J.Y. and W.L.; methodology, X.L.; data curation, X.L. and J.Z.; writing—original draft preparation, X.L.; writing—review and editing, J.Z.; supervision, W.S. and J.Z.; funding acquisition, X.L. and J.Z.; All authors have read and agreed to the published version of the manuscript.

Funding: This study was supported by the National Key Research and Development Program of China (2021YFC2900100), the National Science Foundation of China (41702352), National Pre-research Funds of Hebei GEO University in 2023 (Grant 008), metallogenic regularities and prediction evaluation of strategic metal mineral resources such as lithium and beryllium in eastern China (2019YFC0605202), and mineral geology survey and prospecting prediction in an integrated exploration area (No. DD29190166-2020-08).

Data Availability Statement: All the data are presented in the paper.

Acknowledgments: The authors would like to acknowledge the three anonymous reviewers for their constructive comments, which helped to significantly improve the manuscript.

Conflicts of Interest: The authors declare no conflict of interest.

References

1. Mao, J.; Cheng, Y.; Chen, M.; Pirajno, F. Major types and time-space distribution of Mesozoic ore deposits in South China and their geodynamic settings. *Min. Depos.* **2013**, *48*, 267–294.
2. Mao, J.; Ouyang, H.; Song, S.; Santosh, M.; Yuan, s.D.; Zhou, Z.H.; Zheng, W.; Liu, H.; Liu, P.; Cheng, Y.; et al. Geology and Metallogeny of Tungsten and Tin Deposits in China. *Soc. Econ. Geol. Spec. Publ.* **2019**, *22*, 411–482.
3. Feng, C.; Huang, F.; Zeng, Z.; Qu, W.; Ding, M. Isotopic chronology of Jiulongnao granite and Hongshuizhai greisens-type tungsten deposit in South Jiangxi Province. *J. Jilin Univ. (Earth Sci. Ed.)* **2011**, *41*, 111–121. (In Chinese with English abstract)
4. Wang, D.; Huang, F.; Wang, Y.; He, H.; Li, X.; Liu, X.; Sheng, J.; Liang, T. Regional metallogeny of Tungsten-tin-polymetallic deposits in Nanling region, South China. *Ore Geol. Rev.* **2020**, *120*, 0169–1368. [CrossRef]
5. Zhang, J.; Liu, X.; Zeng, Z.; Li, W.; Peng, L.; Hu, H.; Cheng, J.; Lu, K.; Li, P. The metallogenic epoch and geological implications of the tungsten-tin polymetallic deposits in southern Jiangxi Province, China: Constraints from cassiterite U-Pb and molybdenite Re-Os isotopic dating. *Ore Geol. Rev.* **2021**, *134*, 104159. [CrossRef]
6. Liu, X.; Zhang, J.; Hang, F.; Cheng, J.; Lu, K.; Yang, J.; Wang, M.; Qiu, J.; Wang, Y.; Zhang, X. Tungsten deposits in Southern Jiangxi Province:constraints on the origin of wolframite from in-situ U-Pb isotope dating. *Ore Geol. Rev.* **2022**, *143*, 104774. [CrossRef]
7. Hua, R.; Zhang, W.; Chen, P.; Wang, R. Comparison in the characteristics, origin, and related metallogeny between granites in Dajishan and Piaotang, southern Jiangxi, China. *Geol. J. China Univ.* **2003**, *9*, 609–619. (In Chinese with English abstract)
8. Xiao, J.; Wang, Y.; Hong, Y.; Zhou, Y.; Xie, M.; Wang, D.; Guo, J. Geochemistry characteristics of Xihuashan tungsten granite and its relationship to tungsten metallogenesis. *J. East China Inst. Technol.* **2009**, *32*, 22–31. (In Chinese with English abstract)
9. Lv, K.; Wang, Y.; Xiao, J. Geochemistry characteristics of Xihuashan granite and structural environment discussion. *J. East China Inst. Technol.* **2011**, *34*, 117–128. (In Chinese with English abstract)
10. Feng, C.; Zeng, Z.; Zhang, D.; Qu, W.; Du, A.; Li, D.; She, H. SHRIMP zircon U-Pb and molybdenite Re–Os isotopic dating of the tungsten deposits in the Tianmenshan-Hongtaoling W-Sn orefield, southern Jiangxi Province, China, and geological implications. *Ore Geol. Rev.* **2011**, *43*, 8–25. [CrossRef]
11. Guo, C.; Chen, Y.; Li, C.; Chen, Z.; Lou, F. Zircon SHRIMP U-Pb dating, geochemistry, Sr-Nd isotopic analysis of the Late Jurassic granitoids in the Jiulongnao W-Sn-Pb-Zn ore-concentrated areas in Jiangxi Province and their geological significance. *Acta Geol. Sin.* **2011**, *85*, 1188–1205. (In Chinese with English abstract)
12. Quan, T.; Kong, H.; Wang, G. Petrogenesis of the granites in the Huangshaping area: Constraints from petrochemistry, zircon U-Pb chronology and Hf isotope. *Geotecton. Et Metallog.* **2012**, *36*, 597–606. (In Chinese with English abstract)
13. Guo, C.; Chen, Y.; Zeng, Z.; Lou, F. Petrogenesis of the xihuashan granites in southeastern china: Constraints from geochemistry and in-situ analyses of zircon U-Pb-Hf-O isotopes. *Lithos* **2012**, *148*, 209–227. [CrossRef]
14. Chen, G.; Shu, L.; Shu, L.; Zhang, C.; Ouyang, Y. Geological characteristics and mineralization setting of the Zhuxi tungsten (copper) polymetallic deposit in the eastern Jiangnan Orogen. *Sci. China (Earth Sci.)* **2015**, *45*, 1799–1818. (In Chinese with English abstract) [CrossRef]
15. Wang, X.; Liu, Z.; Liu, S.; Wang, C.; Liu, J.; Wan, H.; Chen, G.; Zhang, S.; Liu, X. LA-ICP-MS zircon U-Pb dating and petrologic geochemistry of fine-grained granite from Zhuxi Cu-W deposit, Jiangxi Province and its geological significance. *Rock Miner. Anal.* **2015**, *34*, 592–599. (In Chinese with English abstract)
16. Guo, C.; Wang, R.; Yuan, S.; Wu, S.H.; Yin, B. Geochronological and geochemical constraints on the petrogenesis and geodynamic setting of the Qianlishan granitic pluton, Southeast China. *Min. Pet.* **2015**, *109*, 253–282. [CrossRef]
17. Li, H.; Palinkas, L.; Watanabe, K.; Xi, X. Petrogenesis of Jurassic A-type granites associated with Cu–Mo and W–Sn deposits in the central Nanling region, South China: Relation to mantle upwelling and intra-continental extension. *Ore Geol. Rev.* **2018**, *92*, 449–462. [CrossRef]
18. Mao, J.; Wu, S.; Song, S.; Dai, P.; Xie, G.; Su, Q.; Liu, P.; Wang, X.; Yu, Z.; Chen, X.; et al. The world-class Jiangnan tungsten belt: Geological characteristics, metallogeny, and ore deposit model. *Chin. Sci. Bull.* **2020**, *65*, 3746–3762. (In Chinese with English abstract) [CrossRef]
19. Wang, Z.; Chen, B.; Ma, X. Petrogenesis of the Late Mesozoic Guposhan composite plutons from the Nanling Range, South China: Implications for W–Sn mineralization. *Am. J. Sci.* **2014**, *314*, 235–277. [CrossRef]

20. Wang, Y.; Fan, W.; Zhang, G.; Zhang, Y. Phanerozoic tec-tonics of the South China Block: Key observations and controversies. *Gondwana Res.* **2013**, *23*, 1273–1305. [CrossRef]
21. Zhong, J.; Chen, Y.; Pirajno, F. Geology, geochemistry and tectonic settings of the molybdenum deposits in South China: A review. *OreGeol. Rev.* **2017**, *81*, 829–855. [CrossRef]
22. Zhong, J.; Pirajno, F.; Chen, Y. Epithermal deposits in South China:Geology, geochemistry, geochronology and tectonic setting. *Gondwana Res.* **2017**, *42*, 193–219. [CrossRef]
23. Gilders, A.; Gill, J.; Coe, R.; Zhao, X.; Liu, Z.; Wang, G.; Yuan, K.; Liu, W.; Kuang, G.; Wu, H. Isotopic and paleomagnetic constraints on the Mesozoic tectonic evolution of south China. *Geo-Phys Res.* **1996**, *101*, 16137–16154. [CrossRef]
24. Chen, Y.; Chen, H.; Zaw, K.; Pirajno, F.; Zhang, Z. Geodynamic settings and tectonic model of skarn gold deposits in China: An overview. *Ore Geol. Rev.* **2007**, *31*, 139–169. [CrossRef]
25. Li, Z.; Li, X. Formation of the 1300-km-wide intracontinen-tal orogen and post-orogenic magmatic province in Mesozoic South China: A flat-slab subduction model. *Geology* **2007**, *35*, 179–182. [CrossRef]
26. Guo, C.; Xu, Y.; Lou, F.; Zheng, J. A comparative study of the Middle Jurassic granodiorite related to Cu and the Late Jurassic granites related to Sn in the Qin-Hang metallogenic belt and a tentative discussion on their tectonic dynamic setting. *Acta Petrol. Miner.* **2013**, *32*, 463–484. (In Chinese with English abstract)
27. Mao, J.; Pirajno, F.; Cook, N. Mesozoic metallogeny in East China and corresponding geodynamic settings—An introduction to the special issue. *Ore Geol. Rev.* **2011**, *43*, 1–7. [CrossRef]
28. Su, H.; Jiang, S.Y. A comparison study of tungsten-bearing granite and related mineralization in the northern Jiangxi-southern Anhui provinces and southern Jiangxi Province in South China. *Sci. China (Earth Sci.)* **2017**, *60*, 1292–1308. (In Chinese with English abstract) [CrossRef]
29. Zhang, J.; Liu, X.; Zeng, Z.; Li, W.; Peng, L.; Hu, H.; Cheng, J.; Lu, K. Age constraints on the genesis of the changkeng tungsten deposit, Nanling region, south China. *Ore Geol. Rev.* **2021**, *134*, 104134. [CrossRef]
30. Lai, Z.; Zhou, Y.; Zeng, Y. Geological Characteristics and Prospecting Prospect of Helong Tungsten Polymetallic Ore Field, Ganxian County, Jiangxi Province. *Adv. Geosci.* **2019**, *9*, 148–158. [CrossRef]
31. Yin, Z.; Zhao, Z.; Tao, J.; Wu, S.; Li, H.; Gan, J.; Chen, W.; Li, X. Deposit geology, geochronology and metallogenic model of Helong W deposit in sou-thern Jiangxi Province. *Acta Pet. Sin.* **2021**, *37*, 1531–1552. (In Chinese with English abstract)
32. Mao, J.; Xie, G.; Li, X. Mesozoic large-scale mineralization and multiple lithospheric extensions from South China. *Earth Sci. Front* **2004**, *11*, 45–56. (In Chinese with English abstract)
33. Mao, J.; Xie, G.; Guo, C. Large-scale tungsten-tin mineralization in the Nanling region, South China: Metallogenic ages and corresponding geodynamic processes. *Acta Petrol. Sin.* **2007**, *23*, 2329–2338. (In Chinese with English abstract)
34. Mao, J.; Xie, G.; Guo, C.; Yuan, S.; Cheng, Y.; Chen, Y. Spatialtemporal distribution of Mesozoic ore deposits in South China and their metallogenic settings. *Geol. J. China Univ.* **2008**, *14*, 510–526. (In Chinese with English abstract)
35. Hua, R.; Chen, P.; Zhang, W. Reviews on the 3 episodic Mesozoic large scale mineralization events in South China. *Miner. Depos.* **2005**, *24*, 99–107. (In Chinese with English abstract)
36. Peng, J.; Hu, R.; Yuan, S.; Bi, X.; Shen, N. The time ranges of granitoid emplacement and related nonferrous metallic mineralization in Southern Hunan. *Geol. Rev.* **2008**, *54*, 617–625. (In Chinese with English abstract)
37. Liu, J.; Zhang, Z.; Wu, Y.; Meng, L.; Shao, F.; Chen, R. Age dating of Dabu pluton and its geological implication in South Jiangxi. *World Nucl. Geosci* **2015**, *32*, 101–106. (In Chinese with English abstract)
38. Fang, G.; Chen, Z.; Chen, Y.; Zhao, Z.; Hou, K.; Zeng, Z. Two petrogenetic stages of Dabu composite granite pluton in South Jiangxi and their geological implications. *Miner. Depos.* **2017**, *36*, 1415–1424. (In Chinese with English abstract)
39. Liang, J.; Qi, F.; Fan, H.; Ding, Y. The geochemical characteristics of Dabu intrusion and the relationship with tungsten mineralization. *China Tungsten Ind.* **2012**, *27*, 7–10. (In Chinese with English abstract)
40. Ludwig, K. *Isoplot/Ex Version 3.00: A Geochronological Toolkit for Microsoft Excel*; Berkeley Geochronology Center: Berkeley, CA, USA, 2003.
41. Andersen, T. Correction of common Pb in U–Pb analyses that do not report ^{204}Pb. *Chem. Geol.* **2002**, *192*, 59–79. [CrossRef]
42. Wiedenbeck, M.; Allé, P.; Corfu, F.; Griffin, W.; Meier, M.; Oberli, F.; Quadt, A.; Roddick, J.; Spiegel, W. Three natural zircon standards for U–Th–Pb, Lu–Hf, trace element and REE analyses. *Geostand. Newsl.* **1995**, *19*, 1–23. [CrossRef]
43. Slama, J.; Košler, J.; Condon, D.; Crowley, J.; Gerdes, A.; Hanchar, J.; Horstwood, M.; Morris, G.; Nasdala, L.; Norberg, N.; et al. Plešovice zircon-a new natural reference material for U–Pb and Hf isotopic microanalysis. *Chem. Geol.* **2008**, *249*, 1–35. [CrossRef]
44. Wu, F.; Yang, Y.; Xie, L.; Yang, J.; Xu, P. Hf isotopic compositions of the standard zircons and baddeleyites used in U–Pb geochronology. *Chem. Geol.* **2006**, *234*, 105–126. [CrossRef]
45. Chu, N.; Taylor, R.; Chavagnac, V.; Nesbitt, R.; Boella, R.; Milton, J.; Germain, C.; Bayon, G.; Burton, K. Hf isotope ratio analysis using multi-collector inductively coupled plasma mass spectrometry: An evaluation of isobaric interference corrections. *J. Anal. At. Spectrom.* **2002**, *17*, 1567–1574. [CrossRef]
46. Blichert-Toft, J.; Albarede, F. The Lu–Hf geochemistry of chondrites and the evolution of the mantle–crust system. *Earth Planet. Sci. Lett* **1997**, *148*, 243–258. [CrossRef]
47. Griffin, W.; Pearson, N.; Belousova, E.; Jackson, S.; Van Achterbergh, E.; O'Reilly, S.Y.; Shee, S.R. The Hf isotope composition of cratonic mantle: LAM-MC-ICPMS analysis of zircon megacrysts in kimberlites. *Geochim. Cosmochim. Acta* **2000**, *64*, 133–147. [CrossRef]

48. Rollinson, H. *Using Geochemical Data: Evaluation, Presentation, Interpretation*; Longman Scientific and Technical: New York, NY, USA, 1993; pp. 1–352.
49. Streckeisen, A.; Le Maitre, R. A chemical approximation to the modal QAPF classification of the igneous rocks. *Neues Jahrb. Für. Mineral. Abh.* **1979**, *136*, 169–206.
50. Sun, S.; McDonough, W. Chemical and isotopic systematics of oceanic basalts: Implications for mantle composition and processes. *Geol. Soc. Lond. Spec. Publ.* **1989**, *42*, 313–345. [CrossRef]
51. Li, C.; Qu, W.; Zhou, L.; Du, A. Rapid separation of osmium by direct distillation with carius tube. *Rock Miner. Anal.* **2010**, *29*, 14–16.
52. McLaren, A.; Gerald, J.; Williams, I. The microstructure of zircon and its influence on the age determination from Pb/U isotopic ratios measured by ion microprobe. *Geochim. Et Cosmochim. Acta* **1994**, *58*, 993–1005. [CrossRef]
53. Booth, M.; Stark, J.; Rastetter, E. Controls on nitrogen cycling in terrestrial ecosystems: A synthetic analysis of literature data. *Ecol. Monogr.* **2005**, *75*, 139–157. [CrossRef]
54. White, L.; Ireland, T. High-uranium matrix effect in zircon and its implications for SHRIMP U–Pb age determinations. *Chem. Geol.* **2012**, *306*, 78–91. [CrossRef]
55. Silver, L.; Deutsch, S. Uranium-lead isotopic variations in zircons: A case study. *J. Geol.* **1963**, *71*, 721–758. [CrossRef]
56. Chakoumakos, B.; Murakami, T.; Lumpkin, G.; Ewing, R. Alphadecay—Induced fracturing in zircon: The transition from the crystalline to the metamict state. *Science* **1987**, *236*, 1556–1559. [CrossRef]
57. Ewing, A.; Mesaros, J.; Gavin, P. Electrochemical detection in microcolumn separations. *Anal. Chem.* **1994**, *66*, 527A–537A. [CrossRef]
58. Williams, I.; Hergt, J. U-Pb dating of Tasmanian dolerites: A cautionary tale of SHRIMP analyses of high-U zircon. In *Beyond 2000: New frontiers in Isotope Geoscience, Lorne, Abstracts and Proceedings*; Woodhead, J.D., Hergt, J.M., Noble, W.P., Eds.; University of Melbourne: Melbourne, Australia, 2000; pp. 185–188.
59. Aikman, A.; Harrison, T.; Hermann, J. The origin of Eo-and Neo-himalayan granitoids, Eastern Tibet. *J. Asian Earth Sci.* **2012**, *58*, 143–157. [CrossRef]
60. Aleinikoff, J.; Wintsch, R.; Fanning, C.; Dorais, M. U–Pb geochronology of zircon and polygenetic titanite from the Glastonbury Complex, Connecticut, USA: An integrated SEM, EMPA, TIMS, and SHRIMP study. *Chemi. Geol.* **2002**, *188*, 125–147. [CrossRef]
61. Sylvester, P. Post-collisional strongly peraluminous granites. *Lithos* **1998**, *45*, 29–44. [CrossRef]
62. Shaw, D. A review of K-Rb fractionation trends by covariance analysis. *Geochim. Cosmochim. Ac.* **1968**, *32*, 573–601. [CrossRef]
63. Irber, W. The lanthanide tetrad effect and its correlation with K/Rb, Eu/Eu*, Sr/Eu, Y/Ho, and Zr/Hf of evolving peraluminous granite suites. *Geochim. Cosmochim. Ac.* **1999**, *63*, 489–508. [CrossRef]
64. Sami, M.; El Monsef, M.A.; Abart, R.; Toksoy-Köksal, F.; Abdelfadil, K.M. Unraveling the Genesis of Highly Fractionated Rare-Metal Granites in the Nubian Shield via the Rare-Earth Elements Tetrad Effect, Sr–Nd Isotope Systematics, and Mineral Chemistry. *ACS Earth Space Chem.* **2022**, *6*, 2368–2384. [CrossRef]
65. Mao, J.; Zheng, W.; Xie, G. Recognition of a Middle-Late Jurassic arc-related porphyry copper belt along the southeast China coast: Geological characteristics and metallogenic implications. *Geology* **2021**, *49*, 1. [CrossRef]
66. Peng, J.; Hu, R.; Bi, X.; Dai, T.; Li, Z.; Li, X.; Shuang, Y.; Yuan, S.; Liu, S. 40 Ar/ 39 Ar isotopic dating of tin mineralization in Furong deposit of Hunan Province and its geological significance. *Miner. Depos.* **2007**, *26*, 237–248. (In Chinese with English abstract)
67. Mao, J.; Chen, M.; Yuan, S.; Guo, C. Geological characteristics of the Qinhang (or Shihang) metallogenic belt in South China and spatial-temporal distribution regularity of mineral deposits. *Acta Geol. Sin.* **2011**, *85*, 636–658, (In Chinese with English abstract).
68. Liu, S.; Wang, D.; Chen, Y.; Li, J.; Ying, L. ^{40}Ar/ ^{39}Ar ages of muscovite from different types tungsten-bearing quartz veins in the Chong-Yu-You concentrated mineral area in Gannan region and its geological significance. *Acta Geol. Sin.* **2008**, *82*, 932–940. (In Chinese with English abstract)
69. Fang, G.; Zhao, Z.; Chen, Y.; Chen, Z.; Krapez, B.; Mao, J. Genetic relationship between granitic magmatism and W mineralization recorded in the Nanling Scientific Drilling (SP-NLSD-2) in the Pangushan W mining district, South China. *Ore Geol. Rev.* **2018**, *101*, 556–577. [CrossRef]
70. Li, X.; McCulloch, M. Geochemical characteristics of Cretaceous mafic dikes from northern Guangdong, SE China: Age, origin and tectonic significance. In *Mantle Dynamics and Plate Interaction in East Asia*; Flower, M.F.J., Chung, S.L., Lo, C.H., Lee, T.-Y., Eds.; AGU Geodynamics: Washington, DC, USA, 1998; Volume 27, pp. 405–419.

Disclaimer/Publisher's Note: The statements, opinions and data contained in all publications are solely those of the individual author(s) and contributor(s) and not of MDPI and/or the editor(s). MDPI and/or the editor(s) disclaim responsibility for any injury to people or property resulting from any ideas, methods, instructions or products referred to in the content.